Ocean Modelling 170 (2022) 101943

Contents lists available at ScienceDirect

Ocean Modelling

journal homepage: www.elsevier.com/locate/ocemod

Validation and inter-comparison of models for landslide tsunami generation

James T. Kirby [a,*], Stephan T. Grilli [b], Juan Horrillo [c], Philip L.-F. Liu [d,o], Dmitry Nicolsky [e], Stephane Abadie [f], Behzad Ataie-Ashtiani [g], Manuel J. Castro [h], Lucie Clous [f], Cipriano Escalante [i], Isaac Fine [j], José Manuel González-Vida [k], Finn Løvholt [l], Patrick Lynett [m], Gangfeng Ma [n], Jorge Macías [h], Sergio Ortega [k], Fengyan Shi [a], Saeedeh Yavari-Ramshe [g], Cheng Zhang [a]

[a] Center for Applied Coastal Research, Department of Civil and Environmental Engineering, University of Delaware, Newark, DE 19716, USA
[b] Department of Ocean Engineering, University of Rhode Island, Narragansett, RI 02882, USA
[c] Department of Ocean Engineering, Texas A&M University at Galveston, 200 Seawolf Parkway, Galveston, TX 77553, USA
[d] Department of Civil and Environmental Engineering, National University of Singapore, Singapore
[e] Geophysical Institute, University of Alaska Fairbanks, 2156 Koyukuk Drive, Fairbanks, AK 99775-7320, USA
[f] Department of Civil Engineering, Université de Pau et des Pays de l'Adour E2S UPPA, SIAME, Anglet, France
[g] Civil Engineering Department, Sharif University of Technology, Tehran, Iran
[h] Facultad de Ciencias, Departamento de Análisis Matemático, University of Málaga, Campus de Teatinos, s/n, Málaga 29080, Spain
[i] Department of Mathematics, University of Córdoba, 14071 Córdoba, Spain
[j] Institute of Ocean Sciences, 9860 West Saanich Road, Sidney, BC V8L 4B2, Canada
[k] Escuela de Ingenierías Industriales, Department of Applied Mathematics, University of Málaga, Campus de Teatinos s/n, Málaga 29071, Spain
[l] Norwegian Geotechnical Institute, P.O. Box 3930, Ullevøal Stadion, 0806 Oslo, Norway
[m] Tsunami Research Center, Sonny Astani Department of Civil & Environmental Engineering, University of Southern California, Los Angeles, CA 90089, USA
[n] Department of Civil and Environmental Engineering, Old Dominion University, Norfolk, VA 23529, USA
[o] Department of Hydraulic and Ocean Engineering, National Cheng Kung University, Tainan City, 70101, Taiwan

ARTICLE INFO

Keywords:
Tsunamis
Landslide tsunamis
Tsunami benchmarks
Landslide tsunami models

ABSTRACT

The Mapping and Modeling Subcommittee of the US National Tsunami Hazard Mitigation Program convened a workshop in January 2017 to evaluate the present state of numerical models for the simulation of tsunamis generated by submarine or subaerial landslides. A range of benchmark tests were provided to participants, with three tests emphasized: (i) a laboratory submarine solid slide in a 2D horizontal tank, (ii) a laboratory submarine granular slide in a 1D flume, and (iii) a field case based on submarine slides which occurred in Port Valdez, AK during the 1964 Alaska earthquake. Nine landslide tsunami models configured with 21 different combinations of physical options were benchmarked, including: (1) hydrostatic models with no frequency dispersion, which include the nonlinear shallow equation models traditionally used for modeling coseismic tsunamis; (2) Boussinesq or one-layer weakly dispersive models; (3) Multi-layer or non-hydrostatic (i.e., dispersive) models; and (4) Full Navier–Stokes models. Model/data comparison indicates that the inclusion of frequency dispersion in model formulations is critical to obtaining physically reasonable results for the test cases considered. Because the importance of dispersive effects is unknown *a priori* for any given simulated event, the central recommendation from this work is that a model with at minimum a leading-order representation of frequency dispersion effects be used whenever possible for landslide tsunami simulations.

1. Introduction

In the past two decades, the United States (US) National Tsunami Hazard Mitigation Program (NTHMP; https://nws.weather.gov/nthmp/) has supported tsunami inundation mapping work involving model simulations from all relevant extreme tsunami sources along all the coastal regions of the US and its territories. While coseismic tsunamis generated by large earthquakes still represent the largest and most significant source of tsunami coastal hazard for most areas in the US, particularly those bordering the Pacific Ocean basin (e.g. Wilson and Torum, 1972; Ichinose et al., 2007; Atlantic and Gulf of Mexico Tsunami Hazard Assessment Group, 2008), tsunamis generated by subaerial or submarine mass failures (referred to collectively here as SMFs, signifying submarine or subaerial mass failures) represent another significant source of hazard for various segments of the US coastline. This has been shown, in particular, for the Gulf of Mexico (Chaytor et al., 2016; Horrillo et al., 2013), Alaska (e.g. Coulter and Migliaccio, 1966; Fine et al., 1998; Fritz et al., 2001, 2009; Weiss

* Corresponding author.
E-mail address: kirby@udel.edu (J.T. Kirby).

https://doi.org/10.1016/j.ocemod.2021.101943
Received 27 July 2021; Received in revised form 20 October 2021; Accepted 26 December 2021
Available online 11 January 2022
1463-5003/

et al., 2009; Nicolsky et al., 2013; Kirby et al., 2016), Hawaii (e.g. Day et al., 2005), Puerto Rico (López-Venegas et al., 2008, 2015), the West Coast (California, Oregon and Washington states) (e.g. Greene et al., 2005; Greene and Ward, 2003) and a large part of the US East Coast (USEC), where many paleo-landslide scars and deposits have been identified on the continental shelf and margin, with the ∼160 km^3 Currituck slide complex, off the coast of North-Carolina being the most prominent one (e.g. Atlantic and Gulf of Mexico Tsunami Hazard Assessment Group, 2008; Geist et al., 2009; ten Brink et al., 2014; Grilli et al., 2015). For the USEC, the most devastating tsunami in recent history was caused in 1929 by an SMF involving a 560 km^3 slump and subsequent debris flow, triggered in the Grand Banks by a M7.2 earthquake (e.g. Fine et al., 2005; Løvholt et al., 2019; Schulten et al., 2019). Besides the risk posed by near-field SMFs (e.g. Geist et al., 2009; Grilli et al., 2015, 2017; Schambach et al., 2019), the USEC faces potential hazard from tsunamis caused by far-field landslides, such as volcanic flank collapses in the Canary Islands (e.g. Ward and Day, 2001; Løvholt et al., 2008; Abadie et al., 2012; Tehranirad et al., 2015). There is also evidence that mega-tsunamis were triggered in the distant past in the Cape Verde Islands (Ramalho et al., 2015) that may have affected the USEC. Volcanic flank collapse, which may affect all young or active volcanic islands, is also a large source of potential hazard for Hawaii (e.g. McMurtry et al., 2004; Day et al., 2005).

Tsunamis triggered by SMFs have occurred all over the world, often with devastating consequences. In the seismically active Mediterranean basin, the 1908 Messina tsunami, caused by a M7.5 earthquake was in part coseismic, but recent work shows that the earthquake triggered a ∼2 km^3 SMF on the flanks of Mount Etna that caused the largest runups (up to 12 m) and destruction in Sicily (Schambach et al., 2020); the combined 80,000 fatalities from the earthquake and tsunami make Messina 1908 the worst natural hazard disaster in modern history in the region. More recently, the 1998 Papua New Guinea tsunami, which was mainly generated by a deep 6–8 km^3 slump triggered by a M7.2 earthquake, inundated the Sissano spit to depths of over 10 m, causing 2000 fatalities (e.g. Tappin et al., 2008; Heidarzadeh and Satake, 2015). The 2018 lateral collapse of the Anak Krakatau volcano, following a long eruptive period, despite being of moderate volume (∼0.22–0.27 km^3) generated 40 m tsunami waves in the near-field that, upon reaching the coast of Java, caused up to 12 m runup and over 450 fatalities (e.g. Grilli et al., 2021, and references therein). The M7.5 2018 Palu earthquake triggered numerous small coastal SMFs (∼0.4–7 10^{-3} km^3) that generated large waves which, combined with the coseismic tsunami, caused extensive destruction along Palu Bay. Combined together, the earthquake and tsunami were responsible for 4300 fatalities (e.g. Liu et al., 2020). Finally, during the 2011 Tohoku tsunami, while the tsunami triggered by the M9 earthquake caused the major destruction, an additional source is needed to explain the 40 m runup that struck the Sanriku coast, and some have proposed that a landslide tsunami was generated by a large and deep SMF triggered by the earthquake near the Japan trench (Tappin et al., 2014). Subaerial landslide tsunamis, including volcano flank collapses represents the most slide events. These includes also the most fatal landslide tsunami event to date, the 1792 Mount Unzen tsunami (Sassa et al., 2016). There have been about ten significant high run-up subaerial landslides events that has taken place within the last decade, such as for instance the 2007 Aysen fjord landslides (Sepúlveda and Serey, 2009), 2014 Lake Askja (Gylfadóttir et al., 2017), the 2015 Taan Fjord tsunami (Higman et al., 2018), and the 2017 Karrat Fjord tsunami (Paris et al., 2019; Svennevig et al., 2020). Further examples can be found in Harbitz et al. (2014).

As evidenced by past historical events, SMF tsunamis, whether triggered by an earthquake or not, can be very devastating and, if they are sourced in the near-field, such as on a continental shelf break, their travel time to shore may be short. Hence, if they reach shore undetected or with little warning, their effects can be made even worse by the lack of time for evacuation. Various works have shown that, independent of the triggering mechanism (Grilli et al., 2009), the size of landslide tsunami waves is primarily a function of SMF volume, initial acceleration (controlled mainly by bottom slope), and submergence depth (e.g. Heinrich, 1992; Harbitz et al., 1993; Grilli and Watts, 1999; Grilli et al., 2002; Grilli and Watts, 2005; Watts et al., 2005; Yavari-Ramshe and Ataie-Ashtiani, 2016; Snelling et al., 2020). To an extent, landslide tsunami waves are also a function of the SMF rheology (Kim et al., 2019; Løvholt et al., 2020). Under certain circumstances, such as when sequential slope failure rates are slow, the material properties have a key control on the tsunamigenic strength (Løvholt et al., 2017). Field studies have shown that SMFs can range from fairly rigid slumps or rotational failures (e.g. Tappin et al., 2008; Løvholt et al., 2019; Schambach et al., 2019, 2020) to debris flows behaving similarly to dense fluids (e.g. Grilli et al., 2019), with a great variety of rheologies in between (e.g. Abadie et al., 2010; Mohammed and Fritz, 2012; Grilli et al., 2017; Si et al., 2018a,b; Kim et al., 2019; Snelling et al., 2020). Additionally, the wavelength L of landslide tsunamis scales with about twice the landslide horizontal dimension in its direction of motion (Watts et al., 2005) and hence can be much shorter than the typically very long wavelength waves occurring in coseismic tsunamis, with correspondingly shorter wave periods (for area-to-volume landslide scaling relationships, see Urgeles and Camerlenghi, 2013). For this reason, landslide tsunamis are often more significantly affected by frequency dispersion effects than are coseismic tsunami waves (e.g. Grilli and Watts, 1999; Grilli et al., 2002; Watts et al., 2003; Grilli and Watts, 2005; Watts et al., 2005; Ma et al., 2012; Glimsdal et al., 2013; Løvholt et al., 2015; Schambach et al., 2019).

In the early development and benchmarking of landslide tsunami models, most investigators concentrated on modeling solid block landslides (e.g. Heinrich, 1992; Harbitz et al., 1993; Grilli and Watts, 1999, 2005; Grilli et al., 2002; Lynett and Liu, 2002; Watts et al., 2003, 2005; Liu et al., 2005), using their own or other laboratory experiments for benchmarking (e.g. Enet and Grilli, 2007; Ataie-Ashtiani and Najafi-Jilani, 2008). In parallel, studies of tsunami generation by deformable slides were carried out either using depth-integrated two-layer model equations (e.g. Jiang and LeBlond, 1992, 1993, 1994; Fine et al., 1998) or by solving 2D or 3D Navier–Stokes equations (e.g., Assier-Rzadkiewicz et al., 1997). These two approaches have led to a newer generation of models used more recently for simulating tsunami generation by deforming slides, represented by a dense fluid or a granular material, some of which will be detailed or applied and benchmarked later in this paper (e.g. Ataie-Ashtiani and Shobeyri, 2008; Weiss et al., 2009; Abadie et al., 2010; Horrillo et al., 2013; Kirby et al., 2016; George and Iverson, 2011, 2014; Ma et al., 2013, 2015; Macías et al., 2015; González-Vida et al., 2019; Løvholt et al., 2017, 2019; Kim et al., 2019; Zengaffinen et al., 2020; Zhang et al., 2021a,b; Macías et al., 2021b). For a comprehensive review of landslide tsunami modeling work through 2016, see Yavari-Ramshe and Ataie-Ashtiani (2016).

As a result of the significant hazard posed by landslide tsunamis for many coastal areas of the US and its territories, and to support the use of numerical models for simulating coastal tsunami hazard and inundation caused by landslide tsunamis, the Mapping and Modeling Subcommittee (MMS) of NTHMP convened a workshop in January 2017 at Texas A& M University, Galveston, Texas, with the goals of evaluating the state of numerical models for the simulation of tsunamis generated by SMF's, and of drawing recommendations for best practice in model selection and modeling of these events. Earlier similar numerical model benchmarking workshops had been organized by NTHMP-MMS in 2011 regarding tsunami runup and inundation (Horrillo et al., 2014) and in 2015 regarding the prediction of tsunami-induced coastal currents (Lynett et al., 2017). NTHMP modelers from different areas of the US as well as international experts were invited to attend. Seven benchmark tests were proposed based on earlier published work, whose data and information were provided to participants ahead of the workshop. Three tests were emphasized that will be detailed in

this paper: Benchmark (2), a laboratory submarine solid slide in a 2D horizontal tank (Enet and Grilli, 2007), Benchmark (4), a laboratory submarine granular slide in a 1D flume (Grilli et al., 2017), and Benchmark (7), a field case based on submarine slides which occurred in Port Valdez, Alaska during the 1964 Alaska earthquake (Nicolsky et al., 2013). During the workshop, nine landslide tsunami models, with 21 different configurations, were submitted for benchmarking and their results presented and discussed by the participants, who are all co-authors of this paper. Models were grouped into four categories based on their treatment of hydrodynamics, and further into four categories based on their treatment of slide rheology, as described below in Section 3.

The workshop is documented online at http://www.udel.edu/kirby/landslide, where the reader may find the final technical report along with write-ups of guest presentations, model descriptions, descriptions of the seven benchmark tests, the provided test data, formatted model results for submitted models, and programs used to conduct the quantitative tests described here in Section 4. Links to the workshop documentation may also be found at https://nws.weather.gov/nthmp/2017MMSLandslide/index.html.

In this paper, we present and discuss results of the three main benchmark tests and lessons learned for modeling best practice for landslide tsunamis. The paper is organized as follows. In Section 2, we detail the three benchmark tests considered. Section 3 summarizes the models that were used in the benchmarking. Section 4 describes the methodology used to compare model results to benchmark data and to each other. Results of the model inter-comparisons as well as comparison with benchmark data are given in Section 5. Section 6 provides conclusions and a discussion of resulting best-practice guidance.

2. Benchmark tests

Participants in the workshop were provided with descriptions and observational results for seven slide configurations, including three laboratory tests with solid slides (Grilli and Watts, 2005; Enet and Grilli, 2007; Liu et al., 2005), three laboratory tests using granular slides (Grilli et al., 2017; Viroulet et al., 2014; Mohammed and Fritz, 2012), and a field case based on slides in Port Valdez, AK during the 1964 Alaska earthquake (Nicolsky et al., 2013). Full descriptions of the benchmarks and associated data sets are available at http://www.udel.edu/kirby/landslide/problems. Participants were asked to provide, as a minimum, results for benchmarks 2, 4 and 7, which are described concisely below.

2.1. Benchmark 2: Three-dimensional rigid submarine slide

2.1.1. Experimental set-up and parameters

This benchmark problem is based on the 3D laboratory experiments of Enet and Grilli (2007). Documentation and data sets provided to workshop participants are available at http://www.udel.edu/kirby/landslide/problems/benchmark_2.html. The experiments were performed in the University of Rhode Island (URI) wave tank of width 3.6 m and length 30 m, with a still water depth of 1.5 m over the flat bottom portion. The model slide slid down a plane slope built in the tank with an angle $\theta = 15°$. A definition sketch is provided in Fig. 1 as well as pictures of the experimental set-up and an example of surface wave generation.

The submarine slide model was built as a streamlined Gaussian-shaped aluminum body with elliptical footprint, with down-slope length $b = 0.395$ m, cross-slope width $w = 0.680$ m, and maximum thickness $T = 0.082$ m (Fig. 1b). The slide shape is defined by

$$\zeta(\xi,\chi) = \frac{T}{1-\epsilon}\max\left[0, \mathrm{sech}(k_b\xi)\mathrm{sech}(k_w\chi) - \epsilon\right] \tag{1}$$

where

$$k_b = \frac{2}{b}\cosh^{-1}\frac{1}{\epsilon}, \qquad k_w = \frac{2}{w}\cosh^{-1}\frac{1}{\epsilon}$$

and where (ξ,χ) are the local down-slope and span-wise coordinates with origin at the slide center. The slide volume is given by

$$V_b = bwT\frac{I_2}{C^2}\left(\frac{I_1/I_2 - \epsilon}{1-\epsilon}\right) \tag{2}$$

with

$$\begin{pmatrix} I_1 \\ I_2 \end{pmatrix} = \int_0^C \begin{pmatrix} F \\ G \end{pmatrix} d\mu$$

$$F(\mu) = \mathrm{sech}(\mu)\tan^{-1}(\sinh G)$$

$$G(\mu) = \cosh^{-1}\left(\frac{\mathrm{sech}\mu}{\epsilon}\right)$$

$$C = \cosh^{-1}\left(\frac{1}{\epsilon}\right)$$

The volume of the fabricated slide was measured to be $V_b = 7.72\times10^{-3}$ m^3, which, using the above equations and slide geometry data, yields $\epsilon = 0.717$, for which the coefficient of V_b in Eq. (2) is 0.3508.

The slide was released at time $t = 0$ from a series of 7 initial submergence depths d (Fig. 1; Table 1). During its motion, the slide was guided by a rail located on the slope/tank axis, using low friction wheels, and slid a short distance (4 mm) above the plane slope. For each submergence depth d, the slide initial abscissa x_i and the abscissa of the slide point of maximum thickness x_g are defined and related by

$$x_g = x_i + T'\sin\theta = \frac{d}{\tan\theta} + \frac{T'}{\sin\theta} \tag{3}$$

with $T' = T + 0.004$ m. The measured slide mass was $M_b = \rho_b V_b = 16.00$ kg, and its bulk density (based on measured volume) was $\rho_b = 2.073$ kg/m^3.

Measured data during each experiment included:

- slide kinematics, obtained from a composite of the slide acceleration measured using a micro-accelerometer embedded within the slide, as well as the time of passage of the slide through three electromechanical gates (see Enet and Grilli, 2007, for details)
- surface elevation at up to four capacitance wave gauges $g1$ to $g4$ (Fig. 2)
- wave runup R (i.e., maximum vertical elevation on the slope) at the tank axis $y = 0$.

Wave gauge $g1$ was located at $(x = x_0, y = 0)$ for each test. The coordinates of gauges $g2$–$g4$ remained fixed for all tests and are given in Table 2.

The measured slide kinematics were found to have a good match with the theoretical law of motion for solid slides (Grilli and Watts, 1999, 2005), given by

$$\frac{S}{S_0} = \ln\left\{\cosh\left(\frac{t}{t_0}\right)\right\} \tag{4}$$

with

$$t_0 = \frac{u_t}{a_0}; \qquad S_0 = \frac{u_t^2}{a_0} \tag{5}$$

being the characteristic time and distance of motion, respectively, defined as a function of the terminal slide velocity u_t and the slide initial acceleration a_0, which are given in turn by

$$u_t = \sqrt{gd}\sqrt{\frac{b\sin\theta}{d}\left(1 - \frac{\tan\psi}{\tan\theta}\right)\frac{(\gamma-1)}{C_d}\frac{2(f^2-\epsilon)}{f-\epsilon}} \tag{6}$$

$$a_0 = g\sin\theta\left(1 - \frac{\tan\psi}{\tan\theta}\right)\left(\frac{\gamma-1}{\gamma+C_m}\right) \tag{7}$$

where g is gravitational acceleration, $\gamma = \rho_b/\rho_w$ is the slide specific gravity, C_m is the slide added mass coefficient, C_d the slide drag coefficient, and $C_n = \tan\psi$, the slide basal Coulomb friction. Based on Eq. (4), for $\epsilon = 0.717$, we find $C = 0.8616$ and $f = 0.8952$. In each experiment, the hydrodynamic coefficients C_m and C_d were calculated as least-square fits, by applying Eqs. (4)–(5) and (6) to the measured slide kinematics, expressed as a composite of center of

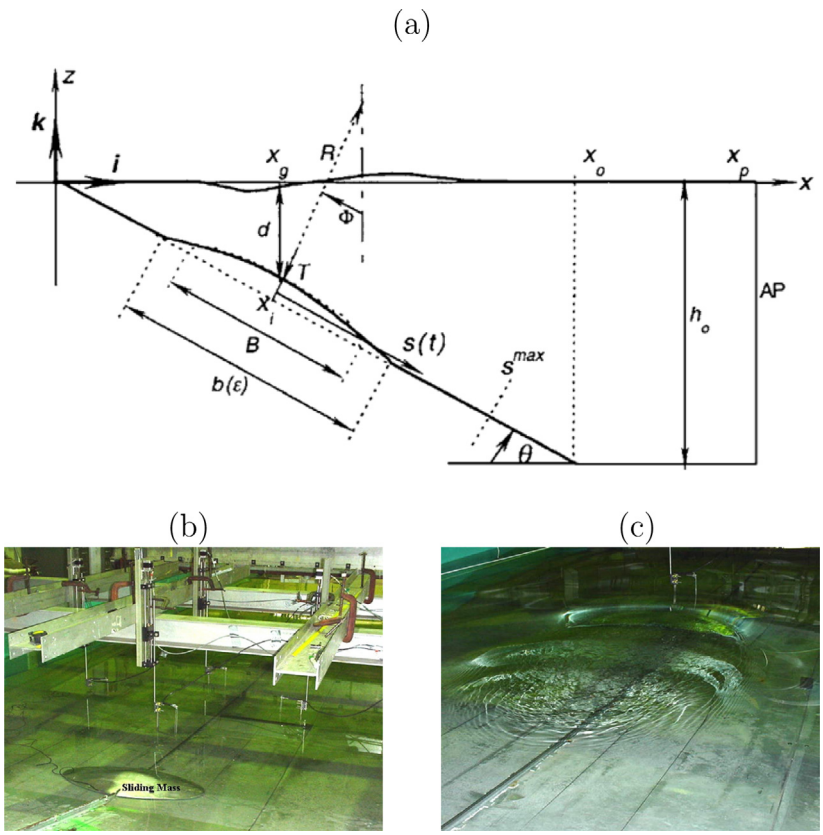

Fig. 1. (a) Sketch of main parameters and variables for wave generation by 3D rigid slide. (b, c) Pictures of experimental set-up and example of surface wave generation, respectively.
Source: Adapted from Enet and Grilli (2007).

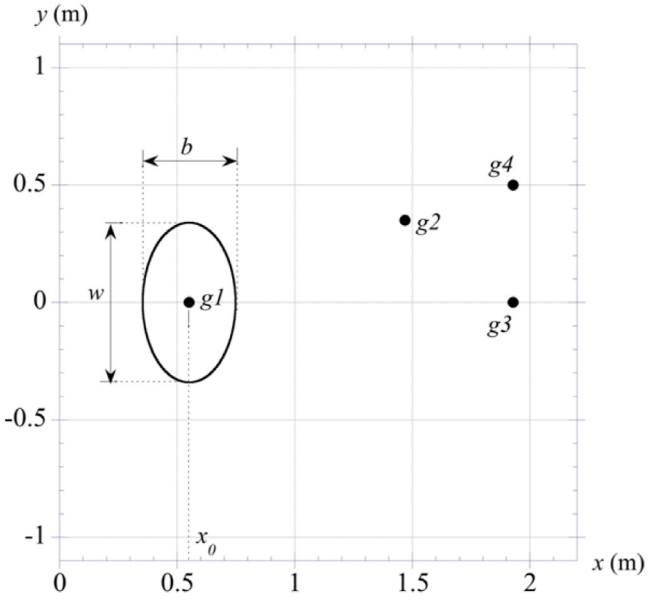

Fig. 2. Wave generation by underwater 3D slide. Landslide and gauge locations are listed in Table 1). Figure is drawn for the case with $d = 61$ mm.
Source: Adapted from Enet and Grilli (2007).

mass acceleration and time of passage at the known position of the 3 electromechanical gates (see Enet and Grilli, 2007, for details). Results are given in Table 1.

Experiments were performed for 7 initial submergence depths d listed in Table 1, together with values of related slide parameters and measured tsunami waves characteristics. Table 1 lists, for each case, the measured characteristic tsunami amplitude η_0 (defined as the maximum depression at gauge g1) and maximum runup on the tank axis R. These small runup values were measured using a digital camera directly viewing the waterline motion over a graduated scale.

Table 1
Wave generation by underwater 3D slide. Measured and curve-fitted slide and wave parameters for various slide initial submergence depths (Fig. 1; adapted from Enet and Grilli, 2007).

d (mm)	61	80	100	120	140	149	189
x_0 (mm) (measured)	551	617	696	763	846	877	1017
x_0 (mm) (theoretical)	560	630	705	780	854	888	1037
η_0 (mm)	13.0	9.2	7.8	5.1	4.4	4.2	3.1
R_u (mm)	6.2	5.7	4.4	3.4	2.3	2.7	2.0
C_m	0.601	0.576	0.627	0.679	0.761	0.601	0.576
C_d	0.473	0.509	0.367	0.332	0.302	0.364	0.353
a_0 (m/s^2)	1.20	1.21	1.19	1.17	1.14	1.20	1.21
u_t (m/s)	1.70	1.64	1.93	2.03	2.13	1.94	1.97
t_0 (s)	1.42	1.36	1.62	1.74	1.87	1.62	1.63
S_0 (m)	2.408	2.223	3.130	3.522	3.980	3.136	3.207

Table 2
Wave gauge locations (x, y) in mm, as indicated in Fig. 2.

$g1$	$g2$	$g3$	$g4$
(x_0,0)	(1469, 350)	(1929, 0)	(1929, 500)

2.1.2. Data provided and benchmark problem

Seven data files were provided to participants which contain, for each of the 7 initial submergence depths (d = 61, 80, 100, 120, 140, 149, 189 mm), the time series of surface elevation measured at up to 4 gages identified as $g1, g2, g3$ and $g4$ (in mm). In each file results are provided for each of two experimental replicates (or runs, marked as *r1* or *r2*), done for the same initial slide parameters, and for their average (marked as *ave*). In some of the tests, data was missing for one of the runs and/or for one of the gages. In the latter case, this is identified in the name tag given each file. For instance, *d61g1234* (*.txt* or *.xls*), indicates that these are results for depth d = 61 mm and gages $g1, g2, g3$, and $g4$. Finally, data files are all provided as tab-delimited text files (with one line of title to skip) and excel spreadsheets. Fig. 3 shows plots of observed surface displacements (in blue) at each gauge for the initial submergence depths of d = 61 and 120 mm. Results from the non-hydrostatic model NHWAVE (Ma et al., 2012, , benchmarked below) configured with a specified bottom motion are shown as red lines for comparison.

To help modelers specify the slide motion, for each experimental case, data files (*kinematics.txt* or *kinematics.xls*) are provided, which contain the average kinematics $t, S(t)$, recalculated for each average experiment using Eqs. (4)–(5) and the values of S_0 and t_0 listed in Table 1, calculated using Eq. (6) and the other data in the table.

The benchmark problem consisted of using the above information on slide shape, density, submergence and kinematics (Table 1), together with reproducing the experimental set-up to simulate surface elevations measured at the 4 wave gages (average of 2 replicates of experiments) as, e.g., shown in Fig. 3, and present similar comparisons of model with experimental results. Participants were requested to provide, as a minimum, results for the two cases illustrated in Fig. 3.

2.2. Benchmark 4: Two-dimensional submarine granular slide

2.2.1. Experimental set-up and parameters

This benchmark problem is based on 2D laboratory experiments of tsunami generation by a submarine slide made of glass beads performed in 2015 by Kimmoun and Dupont in the École Centrale de Marseille (IRPHE) precision tank. Grilli et al. (2017) give the main features of the experiments and http://www.udel.edu/kirby/landslide/problems/benchmark_4.html gives the complete description of the benchmark provided to the workshop participants. These experiments were performed for a series of triangular submarine cavities filled with glass beads, which, upon release by lowering a sluice gate, moved down a planar slope. Figs. 4 and 5 provide pictures and sketches of experimental setup and execution.

Fifty-eight experiments (numbered 13 to 72 in file *Tests_landslide_info.xlsx* available on the website) were performed, each with one replicate for the same parameters. The tank had a width of w = 0.25 m and useful length l = 6.27 m, and was filled with fresh water (density ρ_w = 1000 kg/m^3) to depth h = 0.320 to 0.370 m (Fig. 4). The glass beads had a density ρ_b = 2500 kg/m^3, diameter d_b = 4 or 10 mm, and a total dry weight W_b = 1.5 to 2.5 kg. Upon release by lifting a sluice gate, beads were moving down a slope θ = 35° causing wave generation on the surface (Fig. 5). In 20 of the experiments, a layer of glass beads was glued to the slope. The starting time of experiments t = 0 is defined when the gate has just withdrawn into its cavity (Fig. 4).

During experiments, the deforming slide shape was recorded through the transparent side of the tank with a high-speed video camera (1000 frames per second; see file *benchmark4/test17_video.mp4*) and time series of surface elevations were measured at 4 wave gages, WG1–WG4 (Fig. 4). Fig. 5 shows snapshots extracted from the video of test 17, which has parameters h= 0.330 m; d_b = 4 mm, W_b = 2 kg, and no beads glued on the slope, up to t = 0.60 sec. The snapshots show that due to slide motion "onshore" moving waves are generated that cause runup on the slope with, at the same time, "offshore" moving waves that eventually reflect on the far end of the tank and propagate back towards the generation area. This behavior is also clearly observed in time series measured at wave gages WG1–WG4 (Fig. 6). A detailed analysis of experimental results shows that experiments were highly repeatable with almost unnoticeable differences between surface elevations for 2 replicates.

Grilli et al. (2017) simulated experiments for test 17, corresponding to the case illustrated in Fig. 5, with both the heavy Newtonian fluid-NHWAVE model of Kirby et al. (2016) and the granular slide-NHWAVE model of Ma et al. (2015). Fig. 6 shows the comparison of free surface elevations simulated with the dense fluid model, in which an average slide density ρ_s = 1951 kg/m^3 was used, together with a viscosity μ_s = 0.01 kg/(m.s) and a Manning friction coefficient n = 0.005, specifying friction between the slide and underlying slope. The agreement observed in Fig. 6 between simulations and experiments is quite good. Note, this parameterization of the average slide density and friction parameters is not unique and only provided here as an example. Modelers of this benchmark were free to select the parameters they felt were most appropriate to use for their model. The fluid averaged density was obtained from a weighed average within the triangular cavity of the glass beads and interstitial water density (assuming a random packing); this also led to estimating the initial submergence depth for this case (not measured), to d = 0.0422 m. The selected value of viscosity was based on earlier work by Mendoza and Santamaria-Holek (2009) estimating viscosity for Newtonian granular flows. Finally, once the viscosity selected, the Manning n coefficient value was calibrated for the deforming slide to reach the slide bottom in simulations at the same time as in experiments.

2.2.2. Data provided and benchmark problem

The benchmark here consists in using the above information to simulate, as a minimum, the glass bead experiment of *test 17* and compare the computed surface elevations to those measured at the

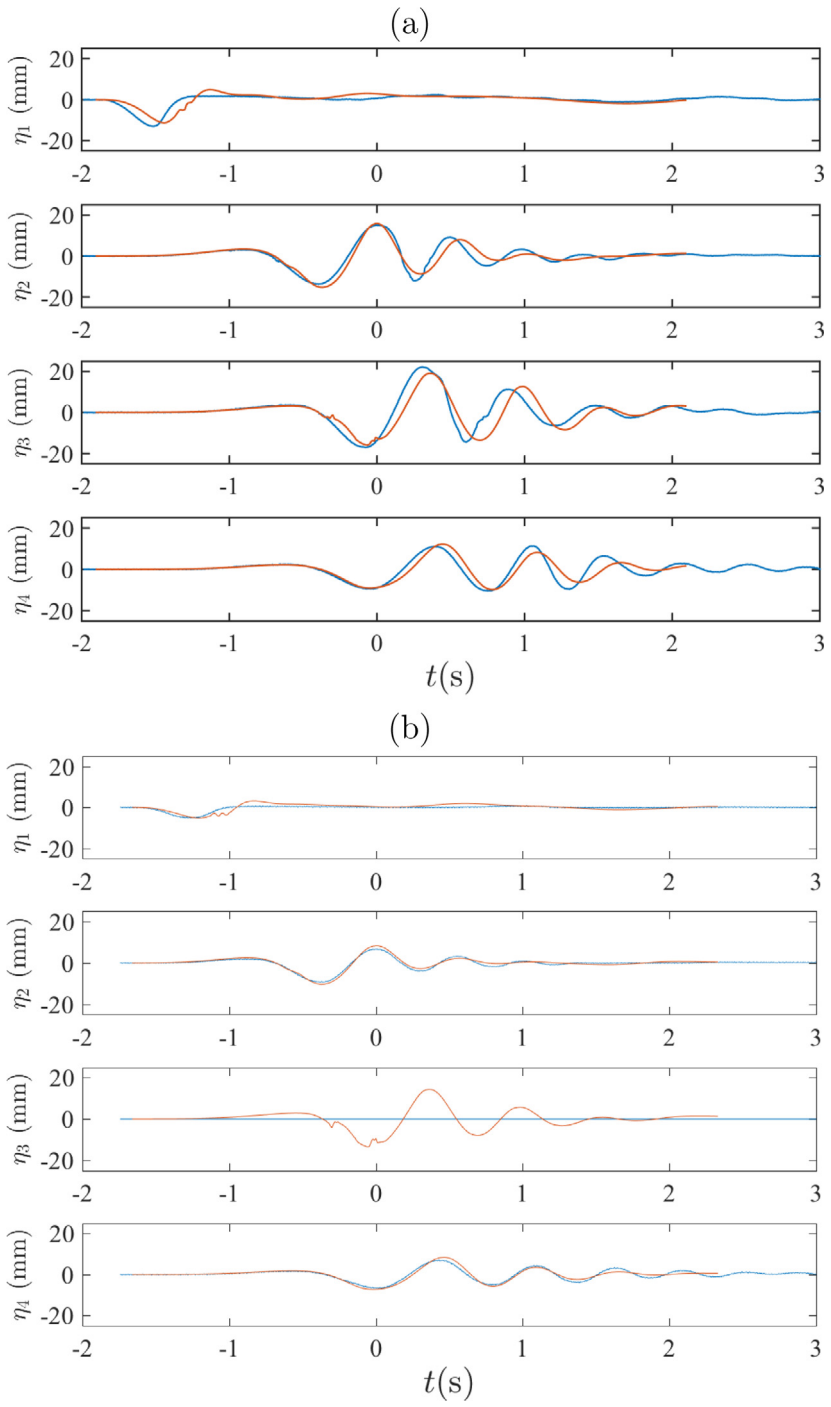

Fig. 3. Observed (blue) and modeled (red) surface elevations at the four gauge locations for Benchmark 2, for initial submergences: (a) $d = 61$ and (b) 120 mm. Model results from Model 1 (NHWAVE, with specified bottom motion). Laboratory data for submergence $d = 120$ mm are not available for gauge 3.

4 wave gauges WG1–WG4 (as in Fig. 6). The measured surface elevations for this test are provided in files *benchmark4/test17.txt* or *benchmark4/test17.csv* and the corresponding high speed video is given in file *benchmark4/test17_video.mp4*. The data is given in format (t(s), η_1 (cm), η_2 (cm), η_3 (cm), η_4 (cm)). The entire set of experimental results for the 58 experiments is provided on the workshop website, with parameters for each test given in file *benchmark4/Tests_landslide_info.xlsx* and the surface elevations measured for each test given in file *benchmark4/gages.zip*, together with a Matlab code to extract and plot the data for each test case. This code also calculates the various dimensions of the slide itself, plus necessary parameters for computations.

2.3. Benchmark 7: Slide at Port Valdez, AK during 1964 Alaska Earthquake

This benchmark problem is based on the historical event which occurred at Port Valdez, AK during the Alaska Earthquake of March 27, 1964 (Coulter and Migliaccio, 1966; Plafker et al., 1969; Wilson and Torum, 1972). Sketches showing the general area, aerial photos before and after the event, the inferred motion of a vessel which broke free of its moorings, and observed runup and debris lines are provided for the region of old Valdez in Appendix B, Figs. B.1–B.3. The event has recently been studied by Nicolsky et al. (2013) and Parsons et al. (2014). The first document provides an overview of the historical

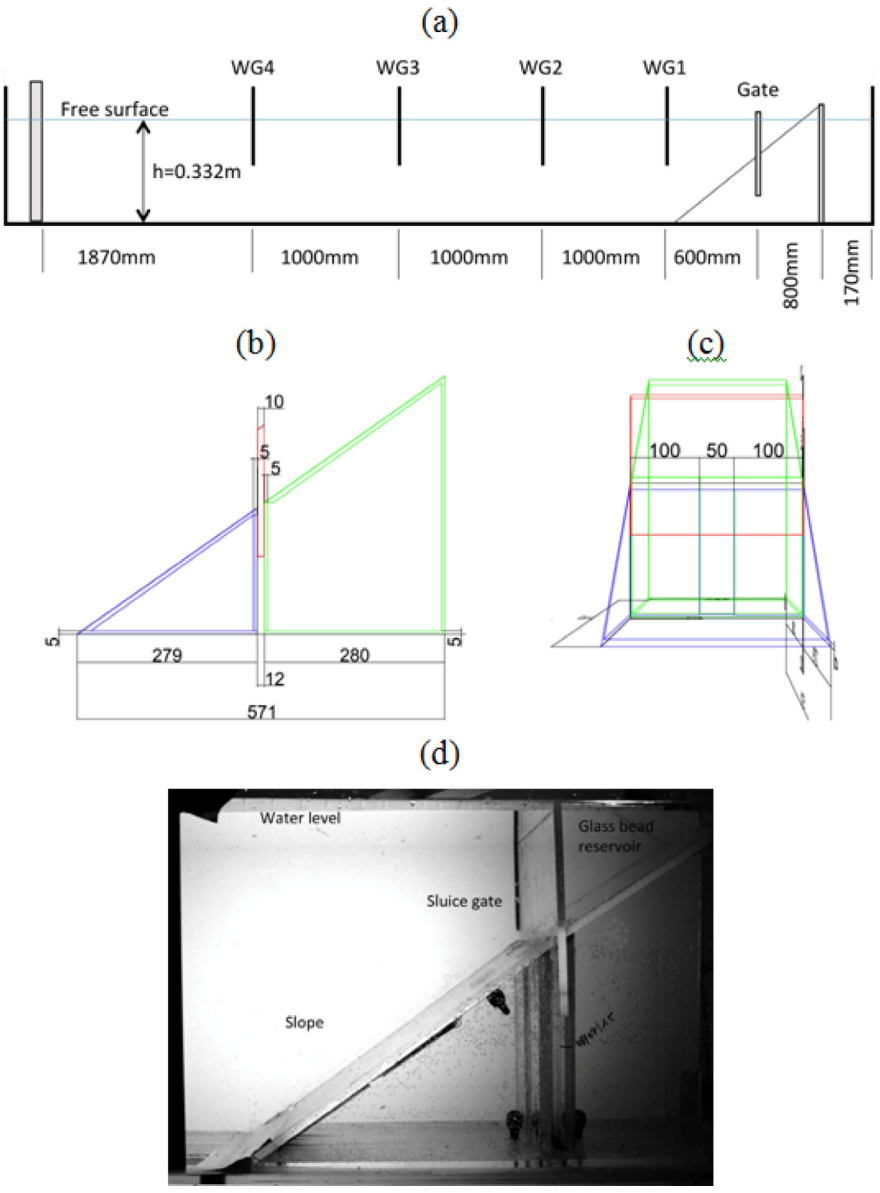

Fig. 4. Set-up for laboratory experiments of tsunami generation by submarine slides made of glass beads performed in IRPHE's precision tank with useful length $l = 6.27$ m, width $w = 0.25$ m, and water depth $h = 0.330$ m. Upon release, beads are moving down a $\theta = 35°$ slope. (a) Longitudinal cross section with marked location of sluice gate and 4 wave gages (WG1, WG2, WG3, WG4). (b,c) Zoom-in on side- and cross-section views of slope and sluice gate (dimensions marked in mm). (d) Picture of experimental set-up around slope and sluice gate (Grilli et al., 2017, Figure 3).

background and geology for the site, and is the principal source for the problem described below. The description of the benchmark provided to participants may be found at http://www.udel.edu/kirby/landslide/problems/benchmark_7.html.

2.3.1. Landslide at the head of Valdez Bay

The largest destruction in Valdez Bay during the M_w9.2 Alaska Earthquake happened in the dock and harbor area, where a massive submarine landslide generated a tsunami, inundating the waterfront up to two blocks inland and causing up to 52 m runup in Port Valdez. The pre- and post-earthquake bathymetry profiles near the site are shown in Coulter and Migliaccio (1966). To the south of Valdez, depth changes exceeding 90 m occurred, which exceeds the depth change off Valdez itself. Thus the major part of the slide took place off the Lowe River delta. It is estimated that approximately 75×10^6 m^3 of unconsolidated deposits were transferred from the waterfront into the bay (Coulter and Migliaccio, 1966). The sequence of tsunami waves following the landslide was reconstructed from eyewitness reports and observations. Hence, there are inherent uncertainties in the resulting estimates of wave time arrivals and wave heights.

The following account of the earthquake is taken from Wilson and Torum (1972) unless otherwise noted. On the evening on March 27, 1964, the 10,815-ton M/V *Chena* was unloading freight at the Valdez dock (Position a in Fig. B.2). The ship initially went astern (Position b) with the water withdrawal that accompanied the initial subsidence of the docks and then the *Chena* heeled to port and rose by 6–9 m on an incoming wave and bottomed at the previous location of the docks (Position c). She then came upright, took another roll to the port and was carried to the small boat harbor (Positions d–e). The *Chena* was momentarily aground with her stern in the wreckage of pilings. Consequently, the *Chena* took a violent roll to the starboard before the boat harbor began to fill with water pouring from the shore. A flux of water from the south filled the boat harbor and carried boats and buildings, dislodged by the first wave, towards the Valdez Hotel. It also lifted the *Chena* and enabled her to float free (Positions e–f). The water began to drain from the boat harbor and the ship came under

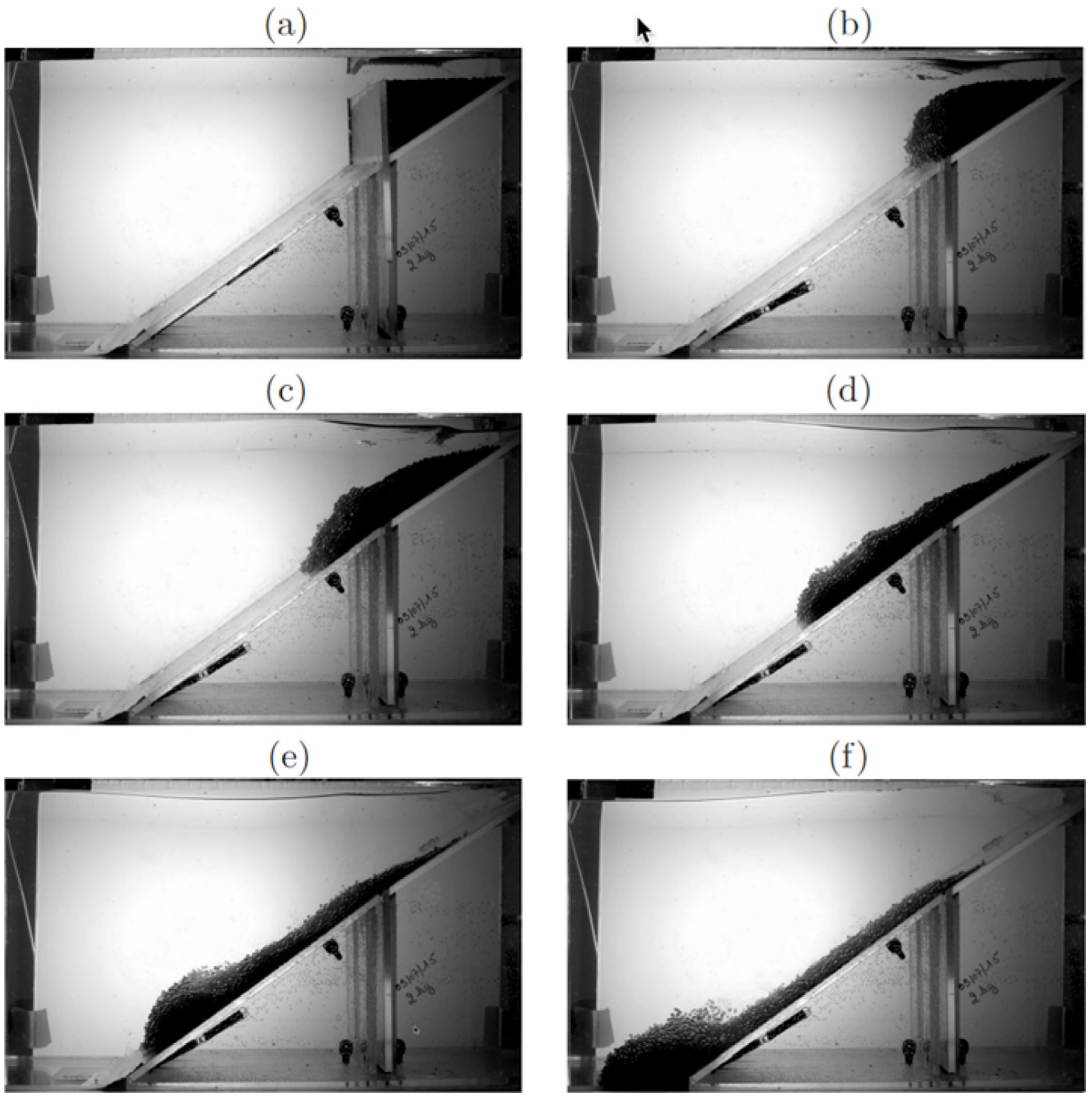

Fig. 5. Snapshots of laboratory experiments of tsunami generation by a submarine slide made of glass beads, for $h = 0.330$ m; $d_b = 4$ mm, $W_b = 2$ kg. Times in each frame relative to gate drop are given by t(s) = (a) −0.105; (b) 0.02; (c) 0.17; (d) 0.32; (e) 0.47; and (f) 0.62. Glass beads are initially stored within the reservoir with the sluice gate up; once the gate is lowered into a bottom cavity (a spring mechanism ensures a swift motion of the gate), the deforming slide moves down the 35° slope, causing wave generation on the free surface. Here, the slope is smooth, with no glued beads. The starting time of experiments $t = 0$ is defined when the gate has just withdrawn into its lower cavity (Grilli et al., 2017, Figure 4).

the influence of a strong southerly current, which carried her close alongshore as in a jet stream (Position f). As the *Chena* was moving south, water was seen cascading over the slide scarp.

The extent of inundation by waves which lifted the *Chena* is hard to constrain based on objective measurements. Some eyewitnesses drove up Alaska Avenue (Fig. B.3) to the corner of McKinley Street in an attempt to reach higher ground, but a large volume of water flowing down the avenue made it impossible to proceed further. They turned right and went to the vicinity of the Standard Oil Company plant, and then turned up Broadway Avenue and proceeded on foot in 0.45 m deep water. Another eyewitness reported that a wave washed onto McKinley Street on the northeast side of town within 5 min after the first shock, and reached two blocks inland. It is thus reasonable to assume that at least two waves flooded the Valdez waterfront and destroyed what was left within two blocks of shore. The runup reached beyond McKinley Street, or about 300 m from the pre-earthquake shoreline at several points.

The second wave crossed the waterfront 10–15 min after the first wave, carrying a large amount of the debris. It has been described as a violent surging wave only slightly smaller than the first. Water from the second wave reached a depth of 0.46 m in the Valdez Hotel on McKinley Street (Wilson and Torum, 1972). The location of the hotel is shown in Fig. B.3 by the red triangle. It is believed that the second wave which flooded the waterfront originated at the other side of the Port Valdez near the Shoup Bay moraine.

2.3.2. Landslide at Shoup Bay moraine

There were no eyewitnesses to waves that struck the shore at other locations along Port Valdez. However, the inundation line was evident from scattered debris and marks on fresh snow. Fig. 7 shows the observed runup around Port Valdez. The highest location obliterated by waves was near the large, abandoned Cliff Mine. According to Plafker et al. (1969), the waves deposited driftwood at points 52 m (170 ft) above sea level and splashed silt and sand up to an elevation of 67 m (220 ft). Directly across from the Cliff Mine in Anderson Bay at the south shore of Port Valdez, the waves ran up to 24 m (78 ft) above the water level and destroyed a small fishing camp. All structures of the camp were swept away, leaving only the driven piling foundations. Its sole inhabitant, Harry Henderson, was missing and presumably drowned in the violent local waves that struck Anderson Bay.

The abandoned Dayville cannery at Jackson Point, 8 km (5 mi) east of Anderson Bay, was also extensively damaged by waves that reached

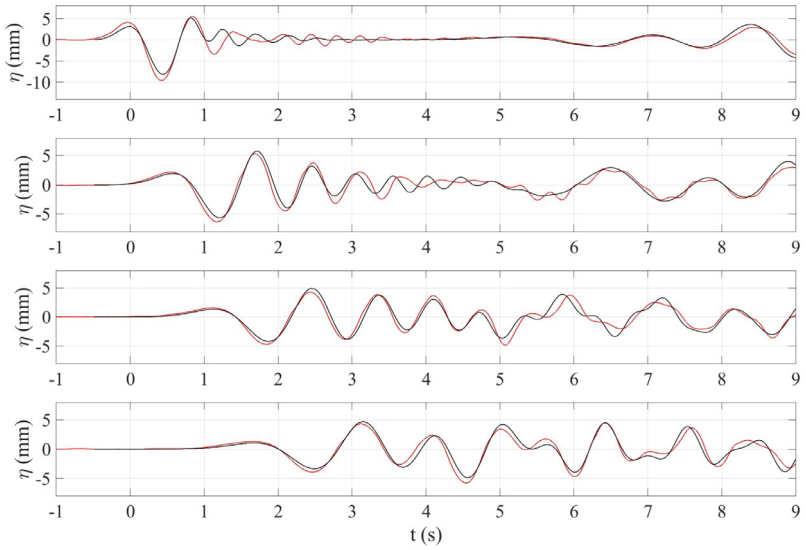

Fig. 6. Experiments of tsunami generation by submarine slides made of glass beads. Comparison of observed (blue) time series of surface elevation at wave gages WG1 to WG4 (Fig. 4a), from top to bottom, to those computed (red) by Grilli et al. (2017) using the model NHWAVE (Ma et al., 2012). Glass beads are represented as a dense Newtonian fluid layer underneath (Kirby et al., 2016) of average density ρ_s = 1951 kg/m^3, dynamic viscosity μ_s = 0.01 kg/(m.s), and bottom friction with a Manning coefficient n = 0.005. The origin of the time axis corresponds to the arrival of the first elevation wave at gage WG1.

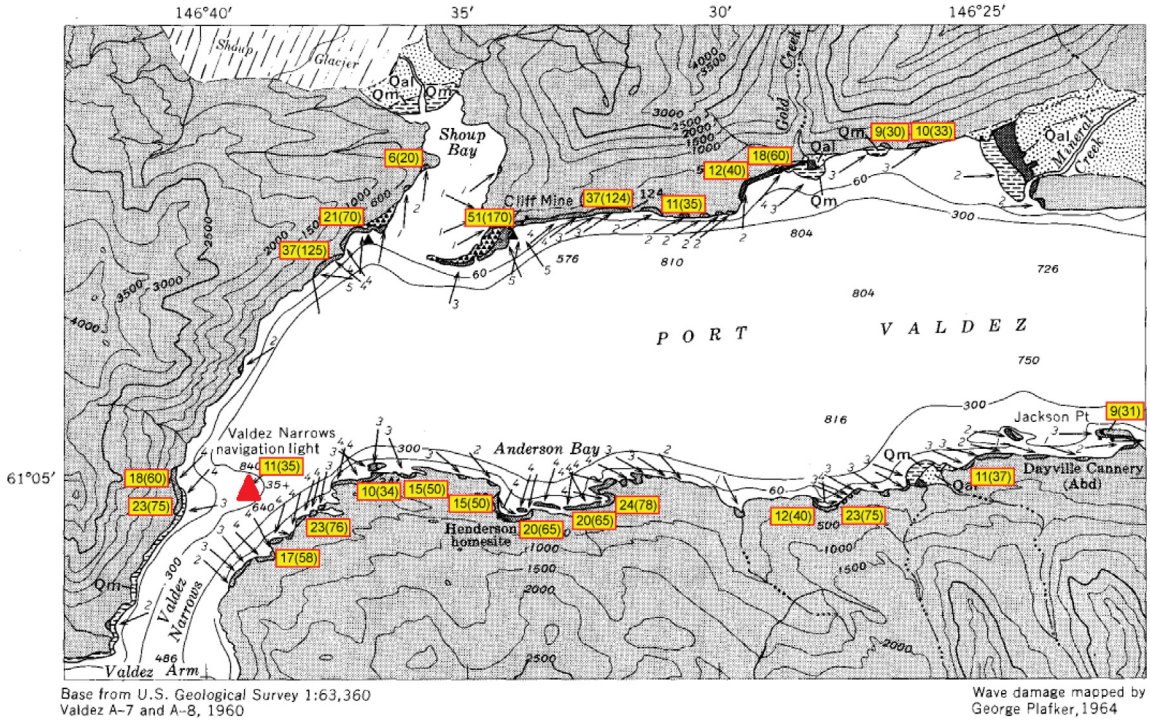

Fig. 7. Impact of the 1964 Alaska Earthquake in Valdez. Distribution and intensity of wave damage in Port Valdez mapped by Mayo and Plafker (as cited in Plafker et al., 1969). Inferred direction of the wave arrival is shown by arrows. Relative magnitude of damage is indicated by a numeral at the base of an arrow, based on the scale: 1-runup about 1–2 m (0–6 ft); 2-runup 8 m (25 ft) on steep shores; 3-maximum runup 17 m (55 ft); 4-maximum runup 21 m (70 ft); 5-maximum runup 52 m (170 ft). Yellow boxed numerals onshore next to shaded areas at edge of water provide runup height in meters (and feet) above sea level at time of the earthquake. The base map and description of the damage are from Plafker et al. (1969).

as high as 9.5 m (31 ft). Elsewhere along the shore, violent waves broke spruce trees with a diameter of 0.6 m (2 ft) at elevations as high as 31 m (101 ft) and deposited barnacle-covered boulders estimated to weigh 760 kg (1700 lb) at points 27 m (88 ft) above the shoreline. The waves that moved westward from Port Valdez overtopped and destroyed the Valdez Narrows navigation light (shown in Fig. 7 by the red triangle) situated on top of a reinforced concrete pedestal 11 m (36 ft) above the lower low water level.

2.3.3. Data provided and benchmark problem

The post-earthquake bathymetry together with the slide thicknesses, shown in Fig. 8, were provided as a single file *benchmark_7_data.zip*. This archive also contains shape files delineating the extent of the observed inundation at the head of Port Valdez and locations of the debris from the first wave. The Matlab script *readData.m* reads all available data and plots contours of the slide thicknesses (Fig. 8a,b) as well as the extent of inundation near the head of Port Valdez (Fig. 8c).

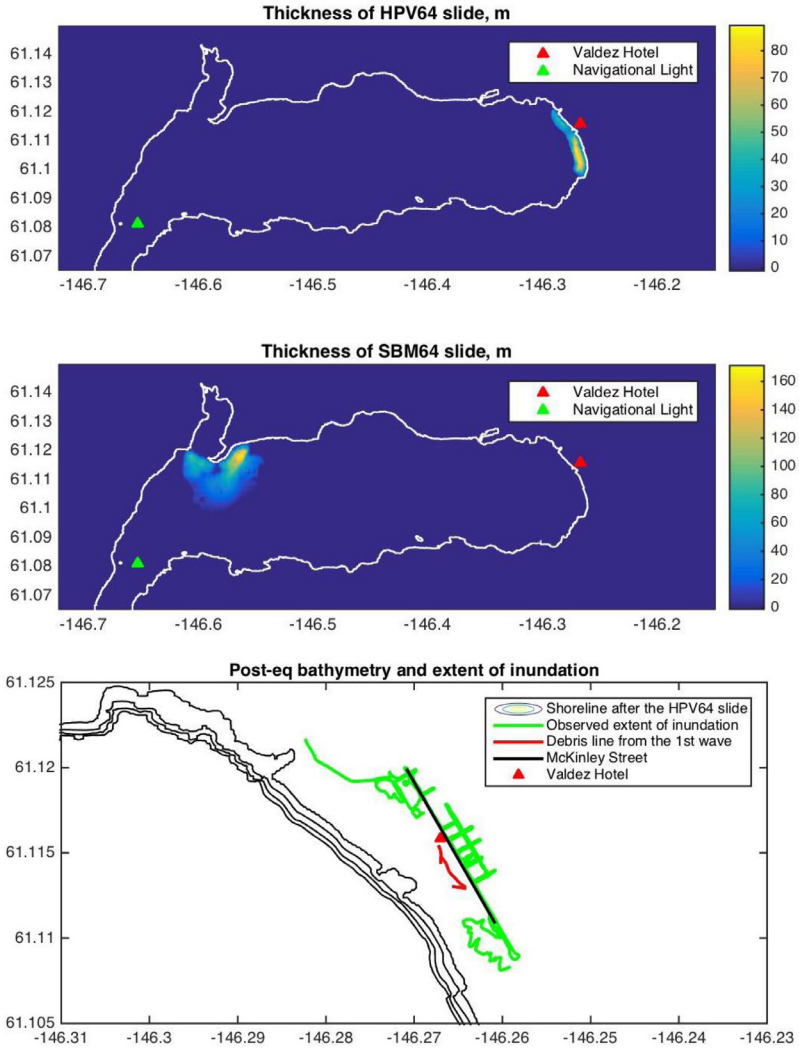

Fig. 8. (a) Reconstructed initial thickness of the old town slide (HPV64) during the 1964 Alaska Earthquake. (b) Reconstructed initial thickness of the Shoup Bay slide (SBM64) during the 1964 Alaska Earthquake. (c) Digitized extent of inundation, locations of the debris and location of McKinley Street.

The benchmark problem here consisted of simulating the extent of inundation for two slide events (at the head of Valdez Bay and at the Shoup Bay moraine), based on before and after bathymetry data, eye-witness observations of the event, and observed runup distribution.

For the slide at the head of Port Valdez (HPV64), it was recommended to

1. reproduce two waves that struck the Valdez waterfront,
2. simulate the extent of inundation reaching at least to McKinley Street.

For the slide at the Shoup Bay moraine (SBM64), it was recommended to

1. simulate the extent of inundation around Port Valdez and reproduce the 20+ m runup at Anderson Bay,
2. simulate the 10+ m wave inundating the navigation light, shown in Fig. 7 by the red triangle, in Valdez Narrows,
3. simulate the 0.5 m wave in the Valdez Hotel, shown in Fig. 8 by the red triangle, located in the head of Port Valdez.

3. Models used in the benchmarking exercise

A total of 9 models were benchmarked as part of the 2017 workshop. Individual documentation for each of the models used is provided at http://www1.udel.edu/kirby/landslide/models.html. Several of the models could be configured in a variety of ways, leading to a total of 21 model configurations listed in Table 3. For the purposes of comparison, the models were grouped into four hydrodynamic configurations, including

1. Hydrostatic models with no frequency dispersion (with results indicated by circles in Figs. 11–14)
2. Boussinesq or one-layer, weakly dispersive models (indicated by 5-pointed stars)
3. Multi-layer or nonhydrostatic models (indicated by 6-pointed stars)
4. Fully-3D Navier–Stokes solvers with surface reconstruction (indicated by asterisks)

Additionally, modeled slide rheology was grouped into four categories including

1 Solid slides (usually an imposed bottom deformation in time; indicated by red symbols)
2 Viscous slides (indicated by green symbols)
3 Granular slides (indicated by blue symbols)
4 3D, continuously varying phase or multiphase (indicated by black symbols).

A brief introduction to each hydrodynamic configuration and treatment of slide rheology is provided in the following two sections. A

Table 3
Models with results submitted for comparison to data.

Model name	Model #	Hydro Type	Slide Type	BM1	BM2-d61	BM2-d120	BM3-case30	BM3-case32	BM4-test17	BM5 Case 1	BM5 Case 2	BM6	BM7	submitted by
data	0			y	y	y	y	y	y	y	y	y	y	
nhwave-s	1	3	1	y	y	y	y	y						UD/ODU/URI
nhwave-v	2	3	2						y				y	UD/ODU/URI
nhwave-g	3	3	3						y	y	y			UD/ODU/URI
globouss-l	4	2	1		y	y								Nor. Geotech. Inst.
globouss-nl	5	2	1		y	y								Nor. Geotech. Inst.
boussclaw-0	6	2	1		y	y								Nor. Geotech. Inst.
boussclaw-15	7	2	1		y	y								Nor. Geotech. Inst.
tsunami3d	8	4	4		y	y			y				y	TAMUG
thetis-newt	9	4	4				y		y	y				U. de Pau
nhwave-3d	10	3	4						y					UD/ODU/URI
thetis-mui	11	4	4							y				U. de Pau
ls3d	12	2	1		y	y							y	Sharif U.
2lcmflow	13	1	3						y	y				Sharif U.
Alaska GI-L	14	1	2		y	y			y				y	U. Alaska
nhwave-s-hydrostatic	15	1	1		y	y								UD/ODU/URI
nhwave-g-hydrostatic	16	1	3						y					UD/ODU/URI
HySEA	17	3[a]	1,3	y	y	y	y	y	y	y	y		y	U. Malaga
fbslide	18	1	1		y	y								IOS
Lynett-nlsw	19	1	1		y	y								USC
Lynett-MSE	21	3	1		y	y								USC

[a] benchmark 7 was carried out using a hydrostatic version of the hydrodynamic model in HySEA.

Hydro Types
0 - data
1 - non-dispersive
2 - weakly dispersive, one layer
3 - nonhydrostatic
4- Navier–Stokes

Slide Types
1 - moving boundary
2 - viscous layer
3 - granular layer
4 - 3D multiphase.

more complete introduction to each model, references to model descriptions in the primary literature, and a description of the range of configurations for each model in the present tests may be found in the individual model write-ups, posted on the workshop website at http://www1.udel.edu/kirby/landslide/reporting.html.

3.1. Treatment of hydrodynamics in models

3.1.1. Non-dispersive models

Models in the non-dispersive category generally solve the Nonlinear Shallow Water Equations (NLSWE). In this class of model, the pressure field is assumed to be hydrostatic with respect to the local water surface, which, for constant water density ρ, gives

$$p = \rho g(\eta - z) \tag{8}$$

where η is the water surface displacement away from rest, and $\eta - z$ represents the distance below the surface. As a result of this simplification, horizontal pressure gradients are depth-uniform, and hence horizontal velocities are uniform over depth if the effects of turbulence and bottom drag are neglected. Models of this type are historically known to be good simulators of runup and inundation, but they can accumulate significant errors when used to propagate waves over long distances or over depths which are not small compared to horizontal wavelengths, as a result of the lack of dispersive effects (Kirby et al., 2013; Schambach et al., 2019). Nevertheless, they have been applied to landslide tsunami modeling (e.g. Harbitz et al., 1993; Fine et al., 1998, 2005; Salmanidou et al., 2017). In the linear limit, waves in this category have the frequency-independent phase speed $c_0 = \sqrt{gh}$, where h is still water depth.

As part of the workshop, the models 2LCMFLOW (Yavari-Ramshe and Ataie-Ashtiani, 2017), ALASKA-GI-L citepnicolsky-etal-pag11, NHWAVE (Ma et al., 2012, 2013, 2015, in hydrostatic mode), HySEA (for benchmark 7 Macías et al., 2015), FBSLIDE and LYNETT-NLSW (Lynett and Liu, 2002) belonged to this category (see Table 3).

3.1.2. Weakly dispersive, Boussinesq-type models

Waves on the surface of finite-depth water have a phase speed c given by

$$c = c_0 \left(\frac{\tanh kh}{kh} \right)^{1/2} \tag{9}$$

where $k = 2\pi/L$ is the wavenumber and L is the corresponding wavelength. For most cases of tsunami generation, propagation and inundation, the dimensionless number kh (or, essentially, the ratio of water depth to wavelength) is relatively small. The limit of $kh \to 0$ recovers the non-dispersive model. The class of weakly-dispersive models (including Boussinesq, Serre and Greene-Naghdi models) retains additional information about c for finite but small values of kh (e.g. Wei et al., 1995; Lynett and Liu, 2002; Watts et al., 2003; Lynett, 2006; Løvholt et al., 2008; Roeber et al., 2010; Shi et al., 2012; Kim et al., 2017). This information is usually related to an asymptotic form of the Taylor series for the added factor in Eq. (9); for example,

$$\frac{\tanh kh}{kh} = 1 - \frac{1}{3}(kh)^2 + O((kh)^4) \tag{10}$$

The corresponding corrections to the horizontal water velocity are usually obtained in the form of a power series in z, and various models may retain higher-order information in powers of kh, or may use series manipulation to obtain rational polynomial forms of Eq. (10) which are more accurate or better behaved for large kh. Models in the following category of dispersive models may be reduced to this form if lowest-order treatments of the model's vertical structure are employed, such as restricting the model to a single vertical layer. See Brocchini (2013) and Kirby (2016) for recent reviews of this class of model.

As part of the workshop, the models GLOBOUS (Løvholt et al., 2008), BOUSSCLAW (Kim et al., 2017) and LS3D (Ataie-Ashtiani and Najafi-Jilani, 2007) belonged to this category (see Table 3).

3.1.3. Dispersive models

Models in this category are essentially solutions of the full hydrodynamic problem under a restrictive set of simplifying assumptions. In particular, the water surface is assumed to be a single-valued function of horizontal position and time. This assumption eliminates the potential for directly describing phenomena such as wave crest overturning during breaking. However, as a result, models in this class do not require the elaborate reconstruction of arbitrary surface geometries employed in more complete Navier–Stokes solvers. The models also typically employ a reduction of the vertical structure of the problem to a finite number of coupled layers, using either low-order approximations of the dynamics in each layer (Stelling and Zijlema, 2003; Bai and Cheung, 2013), or by using differencing stencils applied to the relatively low resolution vertical structure (Ma et al., 2012). These models are reduced to the level of accuracy of Boussinesq models by

reducing the number of vertical layers to one (Yamazaki et al., 2011), or they may approach a full solution of the surface wave problem by allowing the number of vertical layers to be as large as needed. Models for perfect fluid hydrodynamics for surface waves with lengths of kh values appropriate to tsunamis are often adequately described using no more than three vertical layers. Models which solve the fully nonlinear potential flow problem (e.g. Grilli and Watts, 1999; Grilli et al., 2002, 2010) or reproduce the exact linear dispersion relation for narrow-banded waves in slowly varying domains such as the mild-slope equations (Berkhoff, 1972; Smith and Sprinks, 1975) are included in this category. As part of the workshop, the models NHWAVE and HySEA (configured as a multi-layer non-hydrostatic models) and LYNETT-MSE (Bellotti et al., 2008) belong to this category (see Table 3).

3.1.4. Models based on Navier–Stokes solvers

Models in this final category typically solve the full set of Navier–Stokes equations together with boundary conditions applied at an arbitrary, unknown surface (e.g. Heinrich, 1992; Assier-Rzadkiewicz et al., 1997; Popinet, 2003; Liu et al., 2005; Ataie-Ashtiani and Shobeyri, 2008; Weiss et al., 2009; Abadie et al., 2010, 2012; Horrillo et al., 2013). Accurate reproduction of surface geometry requires a great deal of spatial and temporal resolution in the calculation, and hence models of this type typically are expensive to run in terms of time and computer resources.

As part of the workshop, the models TSUNAMI3D (Horrillo et al., 2013), THETIS-NEWT and THETIS-MUI (Clous and Abadie, 2019) belonged to this category (see Table 3).

3.2. Treatment of slide rheology and motion in models

3.2.1. Solid slides

Solid slide motion and geometry are typically specified as a bottom boundary condition, either determined *a priori*, or by applying laws of motion developed for translational and rotational solid slide motions (e.g., Grilli and Watts, 1999; Grilli et al., 2002; Lynett and Liu, 2002; Grilli and Watts, 2005; Watts et al., 2003, 2005; Day et al., 2005). Among the models featured in the workshop, GLOBOUS, BOUSCLAW, LS3D, FBSLIDE and LYNETT belonged to this class of models, with NHWAVE and HySEA having this configuration as an option (see Table 3).

Using this approach, deforming slides with a specified geometry and deformation can also be specified as a bottom boundary condition (Lynett and Liu, 2002; Grilli and Watts, 2005). As is usual for solid slide simulations, there is typically no attempt to couple the slide and water motions dynamically, with the latter only affecting the slide motion through simple coefficients (e.g., drag and added mass coefficients) (Salmanidou et al., 2017).

An exception to this lack of coupling is, for instance, the work of Abadie et al. (2010) who used the multi-material Navier–Stokes model THETIS to simulate both deforming and rigid slides, with the latter represented by a fluid of very high viscosity. With this model, they accurately simulated the solid block experiments of Liu et al. (2005) for both subaerial and submarine cases, without specifying the block law of motion, which was implicitly found in the model through an internal balance of forces.

3.2.2. Deforming slides simulated as dense viscous or viscoplastic fluids

Many early models (e.g., Heinrich, 1992; Harbitz et al., 1993; Assier-Rzadkiewicz et al., 1997; Fine et al., 1998) and some recent models (e.g., Løvholt et al., 2017; Grilli et al., 2019) have simulated tsunami generation by deformable slides by modeling the bottom layer as a dense viscous fluid (Newtonian or non-Newtonian) (e.g., see the recent review by Yavari-Ramshe and Ataie-Ashtiani, 2016). Water motion was either modeled in a single depth-integrated upper layer (two-layer models, e.g., Heinrich, 1992; Harbitz et al., 1993; Assier-Rzadkiewicz et al., 1997; Fine et al., 1998) or in multiple layers (e.g., Kirby et al., 2016; Grilli et al., 2017, and references therein). This motion was coupled to the motion of the bottom layer/slide through dynamic and kinematic equations at the slide-water interface. Depending on model type, water motion was based on solving various sets of equations with different featured physics, from hydrostatic, to non-hydrostatic/dispersive (for example, the two-layer models of Kirby et al., 2016, in which the upper water layer is modeled with the non-hydrostatic σ-coordinate 3D model NHWAVE ma-etal-om12], or full Navier–Stokes (see,e.g., 2D or 3D Navier–Stokes equations to simulate subaerial or submarine slides modeled as dense Newtonian or non-Newtonian fluids by Løvholt et al., 2017; Ataie-Ashtiani and Shobeyri, 2008; Weiss et al., 2009; Abadie et al., 2010, 2012; Horrillo et al., 2013). Among the models featured in the workshop NHWAVE and ALASKA-G-IL belonged to this class of models; THETIS and TSUNAM3D also modeled slides as a dense viscous fluid layer but within a multi-material Navier–Stokes framework (see Table 3).

3.2.3. Slides simulated as saturated granular debris flows

A number of recent laboratory experiments have examined tsunamis generated by subaerial landslides made of gravel (Fritz et al., 2004; Ataie-Ashtiani and Najafi-Jilani, 2008; Heller and Hager, 2010; Mohammed and Fritz, 2012) or glass beads (Viroulet et al., 2014). For deforming underwater landslides and related tsunami generation, 2D experiments were performed by Assier-Rzadkiewicz et al. (1997), who used sand, Ataie-Ashtiani and Nik-khah (2008), who used granular material, and Grilli et al. (2017) who used glass beads.

To simulate such experiments, models have been developed on the same principle as the dense fluid bottom layer, but for a bottom layer representing a granular medium or saturated debris flow (e.g., George and Iverson, 2011, 2014; Ma et al., 2015; Grilli et al., 2017). Another approach to simulate tsunami generation by granular slide or sediment motion has been to simulate flows induced by a varying sediment concentration (e.g., Ma et al., 2013). Among the models featured in the workshop, NHWAVE, HySEA and 2LCMFLOW belonged to this class of model.

For a more comprehensive review of recent modeling work in these areas, see Yavari-Ramshe and Ataie-Ashtiani (2016).

3.2.4. Slides simulated as multiphase components in fully 3D settings

In this implementation, models solving the Navier–Stokes equations in Reynolds-averaged form (together with complete or single-valued representations of water surface geometry), are typically solved for multiple fluids/mediums, one of which is a deforming slide and the other water and air. An example is the multi-material model THETIS by Abadie et al. (2010), which was used to simulate deforming slides in a laboratory set-up or in the field (Abadie et al., 2012). Other examples of this approach are described by Ma et al. (2013), Horrillo et al. (2013) and López-Venegas et al. (2015). To this end, more sophisticated landslide dynamics models are presently being incorporated into full 3D models for landslide-tsunamis, through multi-phase coupled porous-granular rheology (Si et al., 2018a,b; Rauter, 2021). Among the models featured in the workshop, THETIS, TSUNAMI3D and one variant of NHWAVE belonged to this class of model.

4. Analysis approach

This section details the different metrics used in the model-data comparison for each benchmark, with model/data and model/model intercomparisons described in the following section.

4.1. RMS error metrics for time series comparison

RMS error metrics compare the structure of observation and simulation at each gauge location, integrated over time. In order to apply these metrics, it is necessary to interpolate data and model results onto similar discrete time axes. This operation is performed here by interpolating simulation results onto the time axis for observations. The comparison is carried out for each case over a time range corresponding to the existence of useful observational data. Since RMS error estimates for oscillatory signals are also highly sensitive to phase mismatches, the results obtained here are based on shifting simulation results in time in order to obtain a specific synchronization at one of the gauges. In most practical situations, tsunami hazard is not affected by small phase differences, hence simulating an accurate time series in the model is deemed a success, even if there is a small phase shift.

The first error metric represents the square root of the mean square error between observation and simulation results, normalized by the difference between the largest maximum and minimum value of η. This metric is denoted by ϵ^g and is given by

$$\epsilon_j^g = \frac{\sqrt{\sum_i^N (\eta_m(i,j) - \eta_o(i,j))^2}}{\max_i(\eta_o(i,j)) - \min_i(\eta_o(i,j))}; \qquad j = 1 : N_g \tag{11}$$

where N_g is the number of gauges in each experiment and N is the number of points in the time series. A second, alternate RMS error metric denoted ϵ^k is given by

$$\epsilon_j^k = \frac{\sqrt{\sum_i^N (\eta_m(i,j) - \eta_o(i,j))^2}}{\sqrt{\sum_i^N \eta_o(i,j)^2}}; \qquad j = 1 : N_g \tag{12}$$

where the normalization is with respect to the root-mean-square of the observations (standard deviation if the mean is zero), again for each gauge. Results in Section 5 are shown for the first measure Eq. (11). Results based on Eq. (12) are numerically different but were found to be qualitatively similar in pattern; hence they are omitted.

4.2. Statistics of surface displacements

Additional metrics were developed to quantify model reproduction of surface elevation maxima, surface elevation minima, maximum surface wave height, and wave packet variance, which are important for quantifying various aspects of tsunami hazard:

- Maximum surface displacement for a single gauge, normalized by observed values

$$\epsilon_j^{(1)} = \mathrm{Max}_i(\eta_m(i,j))/\mathrm{Max}_i(\eta_o(i,j)); \qquad j = 1 : N_g \tag{13}$$

- Minimum surface displacement for a single gauge, normalized by observed values

$$\epsilon_j^{(2)} = -\mathrm{Min}_i(\eta_m(i,j))/\mathrm{Min}_i(\eta_o(i,j)); \qquad j = 1 : N_g \tag{14}$$

- Total surface excursion for each gauge, normalized by the maximum observed surface excursion

$$\epsilon_j^{(3)} = [\mathrm{Max}_i(\eta_m(i,j)) - \mathrm{Min}_i(\eta_m(i,j))]/[\mathrm{Max}_i(\eta_o(i,j)) - \mathrm{Min}_i(\eta_o(i,j))]; \qquad j = 1 : N_g \tag{15}$$

- Total variance for each gauge, normalized by observed variance for each gauge

$$\epsilon_j^{(4)} = [\sum_{i=1}^N \eta_m(i,j)^2]/[\sum_{i=1}^N \eta_o(i,j)^2]; \qquad j = 1 : N_g \tag{16}$$

4.3. Wavelet analysis of transient wave packets

Tsunami events typically consist of finite-length packets of waves with rapidly varying frequency and amplitude. An analysis of the distribution of amplitude and frequency in space and time can be revealing of the underlying fluid mechanics governing the propagation of the waves. In particular, we can examine the effects of frequency dispersion, or non-hydrostatic behavior, on the advancing wave. This analysis needs to be carried out using a framework that is appropriate for describing non-stationary behavior of the analyzed signal, and it is performed here using the Continuous Wavelet Transform (CWT) (see Addison, 2018, for a recent overview). The description of the CWT is well established but may be unfamiliar to some readers, and so a description of the basics is provided as Appendix A.

To illustrate the application of the CWT to a tsunami signal, we show in Fig. 9 the modulus of the transform $|T(t,f)|$ as a function of frequency and time for Benchmark 2, $d = 61$ mm data (Table 1). Solid red curves show the locus of times at which the maximum of $|T|$ occurs at each frequency f. The panel for Gauge 3 (Fig. 9c) shows two additional curves. For Benchmark 2, Gauge 3 (g3 in Fig. 2) is located downslope in the direction of landslide travel. A wave with frequency f traveling in this direction from location x_1 to x_3 would traverse this distance in a time interval

$$t_3 - t_1 = \int_{x_1}^{x_3} \frac{dx}{c^*(h(x),f)} \tag{17}$$

where depth h varies in x and where the local speed of propagation $c^*(h,f)$ depends on h and, in the case of dispersive motion, frequency f. Two relevant speeds based on linear wave theory are the phase speed c and the group velocity c_g, given in terms of wavenumber $k = 2\pi/L$ (where L is wavelength) by

$$c^2 = \frac{g}{k}\tanh kh; \qquad c_g = \frac{c}{2}\left(1 + \frac{2kh}{\sinh 2kh}\right) \tag{18}$$

with $g = 9.806$ m/s^2 being gravitational acceleration. In the long wave limit ($kh \to 0$), both c and c_g are asymptotic to $\sqrt{gh}$, and dependence on frequency is lost. In this limit, all wave components in a multi-component wave train would travel at the same speed. This is the non-dispersive limit, characteristic of either linear or nonlinear shallow water equations.

In Fig. 9a, the nearly vertical red line represents the location of the initial packet during the drawdown process. A reference frequency $\omega_0 = 5$ (see Eq. (A.8) in Appendix) was used. For Gauge 3, the red dashed line represents replacing c^* in Eq. (17) by group velocity c_g, while the dotted red line represents replacing c^* by phase speed c. Intrinsically, we would expect the propagation of the energy content at each frequency to be governed by the group velocity, so that the solid red line and dashed red line would coincide. Several factors keep this from being apparent in this case. First, the slide is present in the domain during the propagation process, and thus phase speed or group velocity are affected by a time-varying bottom geometry and are not straightforward to interpret. More important, however, is a processing artifact which reduces the apparent arrival time when the wavelet width is adjusted to improve time localization. Relaxation of this constraint in favor of improving frequency localization leads to better estimates of arrival time, since the estimate at each frequency is less contaminated by neighboring frequencies in the strongly dispersive cases considered.

This effect is illustrated in Fig. 10, for time series measured at Gauge 3 (WG3) in Benchmark 4 (Figs. 3 to 6); results for the wavelet transform are shown in the figure for a scaled reference frequency $\omega_0 = 5$ or 15. The improvement in agreement with linear theory and propagation at the group velocity is apparent. Since this result is expected and should be intrinsic to all the cases considered here, we show all results in Section 5 in terms of wavelets with higher temporal resolution. We utilize arrival times at each gauge and frequency in model/data comparisons, in order to assess the accuracy of models to represent propagation at each component frequency.

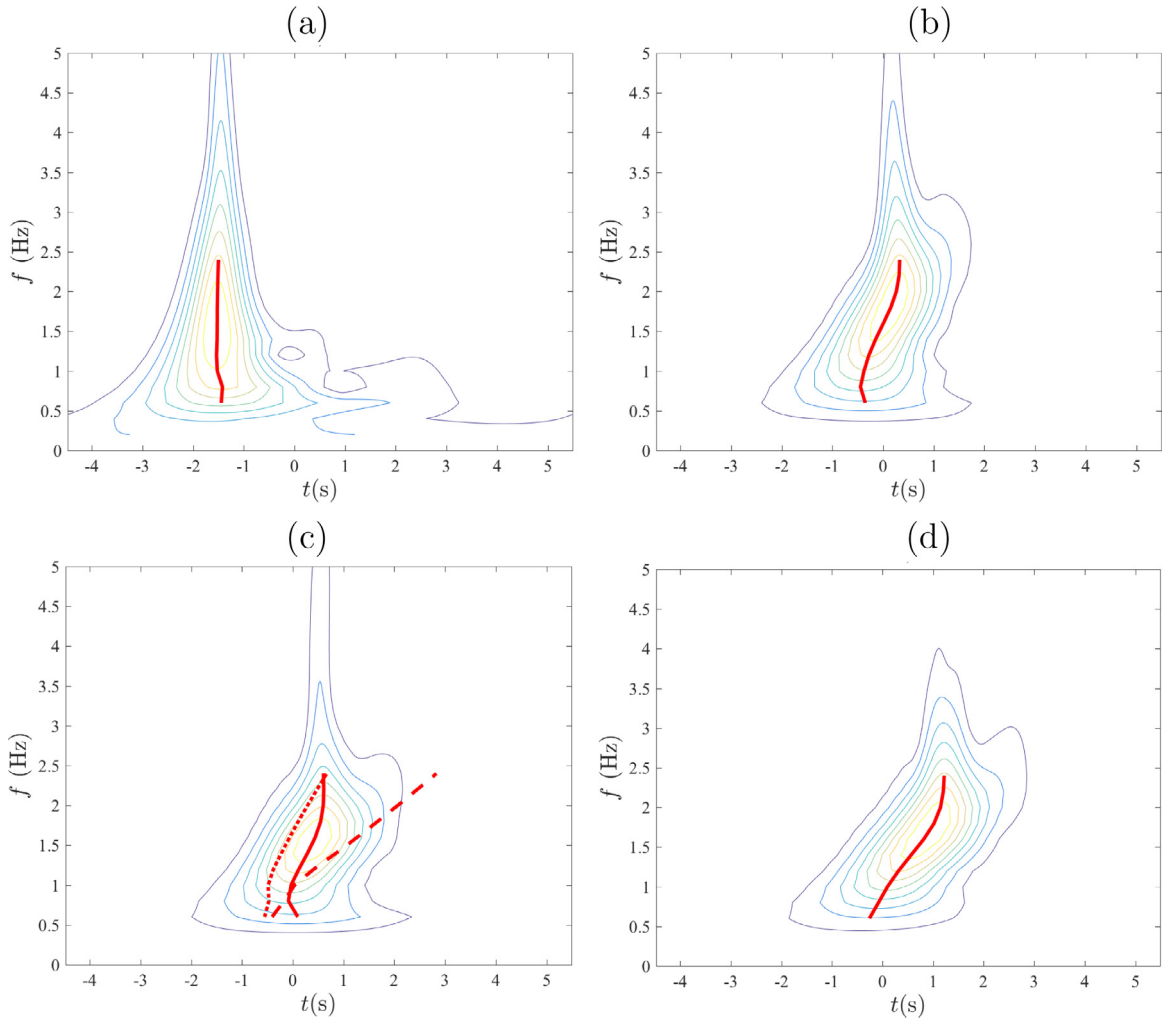

Fig. 9. Benchmark 2, $d = 61$ mm (Table 1), modulus of wavelet transform $|T|$ of measured surface displacements at gauges: (a–d) 1–4 (g1 to g4 in Fig. 2). Solid red curves are locus of maximum $|T|(t)$ at each frequency f. In (c), the red dashed line represents replacing c^* in Eq. (17) by group velocity c_g, while the dotted red line represents replacing c^* by phase speed c.

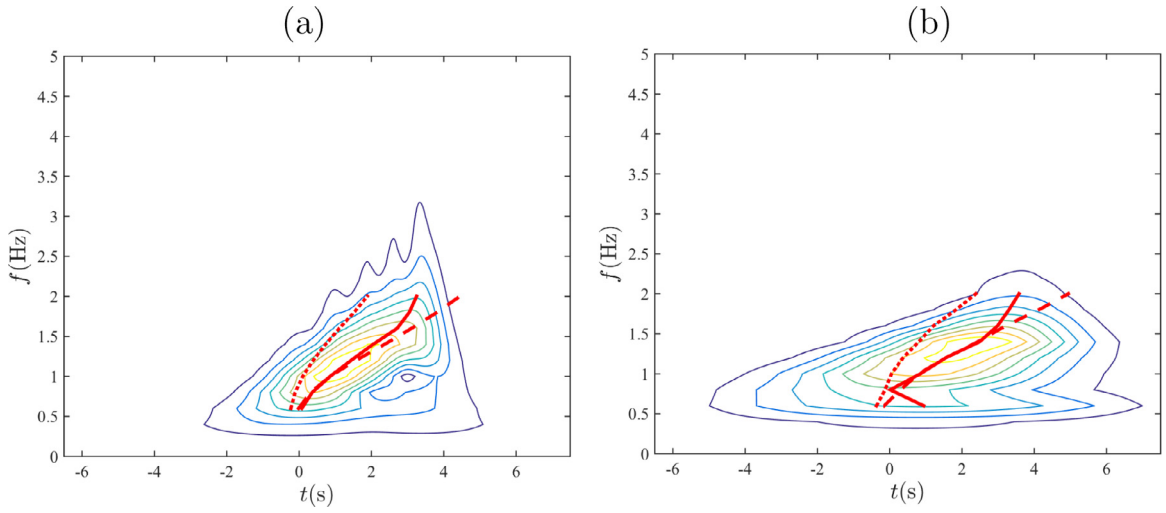

Fig. 10. Benchmark 4 (described in Figs. 4 to 6). Moduli $|T|$ of wavelet transforms and estimated arrival times at Gauge 3 (WG3) for two choices (a) $\omega_0 = 5$ and (b) $\omega_0 = 15$, illustrating a tradeoff between time and frequency localization controlled by that parameter (see Eq. (A.8)).

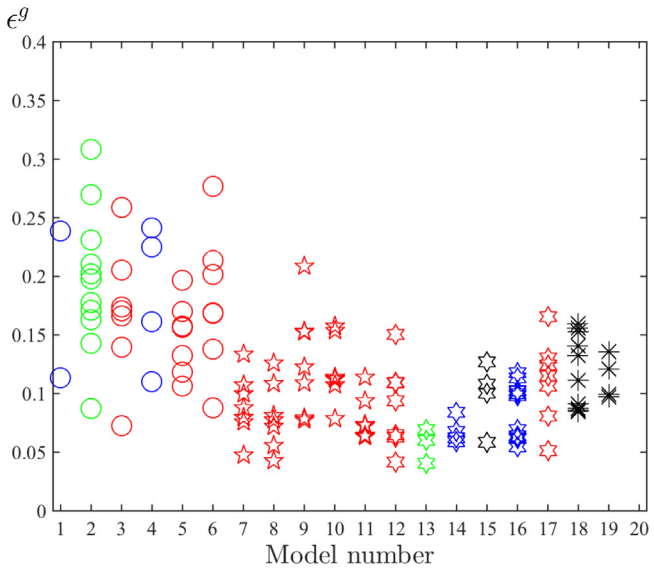

Fig. 11. Distribution of RMS errors ϵ^g by model for all gauges and all considered cases for Benchmarks 2 and 4. Results are grouped here according to model treatment of hydrodynamics. Numbering on the bottom axis does not correspond to the list in Table 3. Symbols indicate: (○) hydrostatic models, (☆) weakly dispersive models, (✡) dispersive (non-hydrostatic) models, (∗) Navier–Stokes models. Colors indicate treatment of slide material, including (red) solid slides, (green) viscous slides, (blue) granular slides, and (black) multiphase models.

5. Model-data comparisons

In this section, we evaluate the performance of all submitted model results for Benchmarks 2 and 4 using the methods described in Section 4. We then provide a more qualitative analysis of results for Benchmark 7, where model results are subject both to the choice of model and the modeler's subjective treatment of information related to the provided input data.

5.1. Data sources

See http://www1.udel.edu/kirby/landslide/reporting.html for data needed to reconstruct the results shown here. In particular,

1. http://www1.udel.edu/kirby/landslide/report/formatted_results.zip provides data in a common format. Files in the unzipped folder are Matlab .mat files, each containing a single data array with dimension (N by 5). For Benchmarks 2 and 4, the array columns contain time (s) and surface displacements at gauges 1–4 (mm). For Benchmark 7, the files are in a similar format, with columns 2–5 displaying elevations at the Navigation Light, Old Valdez Hotel, Point 37 and Point 38, all in meters (m).
   Each file name follows the following convention: *bmX_mY_NOTE.mat*, where X denotes the benchmark number (2, 4 or 7) and Y denotes the model number, as indicated in Table 3. Possible NOTEs are "d061" or "d120" for the two depths of submergence in Benchmark 2, or "case1" for Benchmark 4, which indicates the data set Test17 and was the only case used here. For each case in Benchmarks 2 and 4, model number X = 0 indicates the observed data, reformatted into the same common format. Time series of observed data do not exist for Benchmark 7.
   Finally, the folder contains submitted results for several of the models for Benchmarks 3 and 5. These results are provided for inspection, but are not analyzed or otherwise represented in the final technical report for the workshop or in this paper.
2. http://www1.udel.edu/kirby/landslide/report/errors.zip provides a table of results for the individual model RMS errors (with models listed as indicated in Table 3) in the file *error_data.mat* (Eq. (11)), and for the surface elevation errors in the file *error_heights.mat* Eq. (13)–(16)).
3. http://www1.udel.edu/kirby/landslide/report/programs.zip contains the Matlab scripts used to carry out data analysis and model/data comparisons. These scripts were written by the first author JK (except for portions of the script for Benchmark 7, provided by the fifth author DN) and are in the public domain. The readme file in the zipped folder provides a complete table of contents for the scripts used.

We note that the presentation of results by model number in Figs. 11–14 does not correspond to the numbering of models in Table 3, where the models are not grouped in terms of hydrodynamic or rheological choices. Data are grouped according to the choice of hydrodynamic formulation in Figs. 11–14 in order to accentuate the consistency of results within each of the four groups. The correspondence to individual models, as listed in Table 3, is preserved in the filenames for the .mat files as indicated above.

5.2. RMS error metric

We first consider the distribution of RMS errors for each gauge as given by the error metric ϵ^g defined in Eq. (11). In order to emphasize consistency between model types, we provide results here without regard to the performance of individual models. The reader may reconstruct these correspondences, if desired, by looking up individual error estimates in the files *error_data.mat* and *stuff.mat*, where the errors are listed with model numbers corresponding to entries in Table 3. The metric ϵ^g describes a normalized RMS error based on comparison of the modeled and observed time series at each measurement location. Results of this test are shown in Fig. 11, where ϵ^g for each model is presented without reference to gauge location and for both Benchmarks 2 and 4. The results show a clear tendency towards decreasing error for models with more accurate dispersion properties. Non-dispersive hydrostatic models show a tendency towards a much higher RMS error, with values up to 2 to 3 times higher than the next most accurate category, the weakly dispersive models represented by Boussinesq-type models. Models in the last three categories (weakly-dispersive, dispersive, and Navier–Stokes) are generally consistent with each other, with RMS error measures of around 0.1. The most accurate simulations were for model 13, which represented a non-hydrostatic model run for Benchmark 4 with viscous slide rheology. In general, the dispersive models slightly outperformed the weakly-dispersive models, which

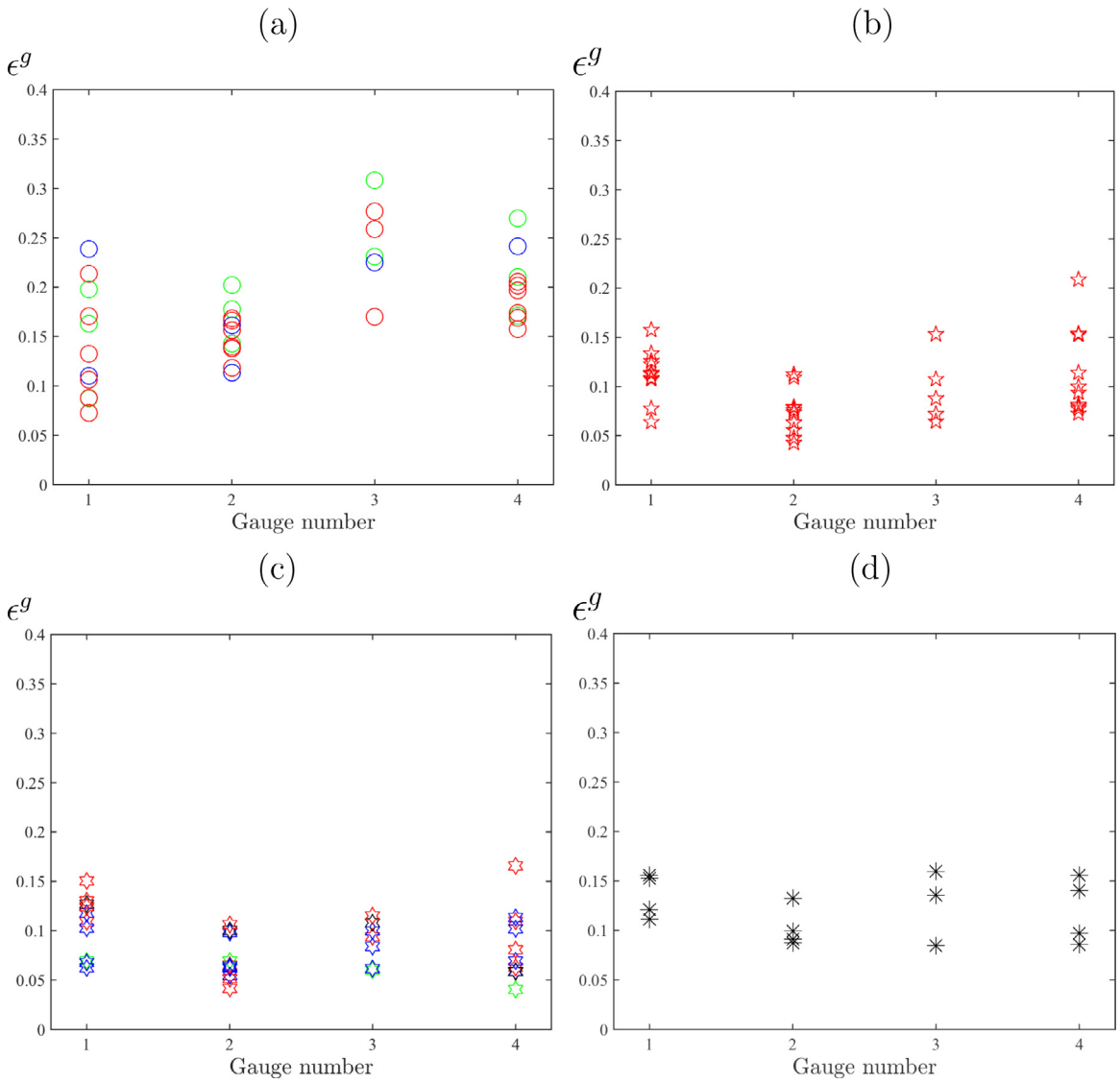

Fig. 12. Distribution of RMS errors ϵ^g by hydrodynamic model type for each gauge in Benchmarks 2 and 4 (g1–g4 or WG1–WG4). (a) Hydrostatic models, (b) Boussinesq models, (c) Non-hydrostatic models, (d) Navier–Stokes/VOF models. See Fig. 11 caption for symbol definition.

could be expected. They also outperform the Navier–Stokes solvers, which could be due to limitations in the handling of slide rheology properties in a fluid continuum. Overall, however, this figure does not provide a dramatic sorting of the 3 types of models which incorporate some degree of frequency dispersion in the treatment of the surface wave as they all perform reasonably well.

Fig. 12 shows the RMS error ϵ^g for all gauges in Benchmarks 2 and 4, sorted by hydrodynamic model type. The most dramatic result here is again the distinction between hydrostatic models and the remaining three categories, with the hydrostatic models showing systematically higher error at all gauge locations. Fig. 12 also shows a distinction between Boussinesq models (Panel b) and the remaining categories of dispersive models, with Boussinesq models showing an increasing error with distance away from the source region, whereas non hydrostatic and Navier–Stokes models give a fairly constant level of error across all four gauge locations due to the accurate representation of dispersion.

Finally, Fig. 13 separates the RMS error ϵ^g for Benchmarks 2 (with a solid slide) and 4 (with a granular slide). Models performed comparably on each benchmark, with the hydrostatic models showing the greatest error in either case.

5.3. Surface displacement error metrics

Fig. 14 shows the surface displacement error metrics defined in Eqs. (13)–(16), computed based on all benchmarked model results (Table 3), for the 4 gauges in Benchmarks 2 and 4.

Fig. 14a shows the normalized maximum surface elevations $\epsilon_j^{(1)}$ (Eq. (13)) and normalized minimum surface elevations $\epsilon_j^{(2)}$ (Eq. (14)), for $j = 1, \ldots, 4$. Hydrostatic models all show large negative minimum value of the error metrics, associated with the large surface drawdown occurring over the moving slide in hydrostatic simulations (see, e.g., Fig. 17c for Model 14 for a dramatic example of this effect for Benchmark 7). Almost all cases with a large overprediction of maximum elevation are associated with Benchmark 2, gauge 1, where positive surface displacements in the experiment are generally quite small. Aside from these anomalies, the models with some representation of frequency dispersion perform adequately and in a fairly uniform manner, with each category outperforming the hydrostatic models.

Fig. 14b shows $\epsilon_j^{(3)}$ (Eq. (15)), which indicates how well total surface excursion is simulated over the entire generated wave packet, and $\epsilon_j^{(4)}$ (Eq. (16)), which indicates how well the packet total variance

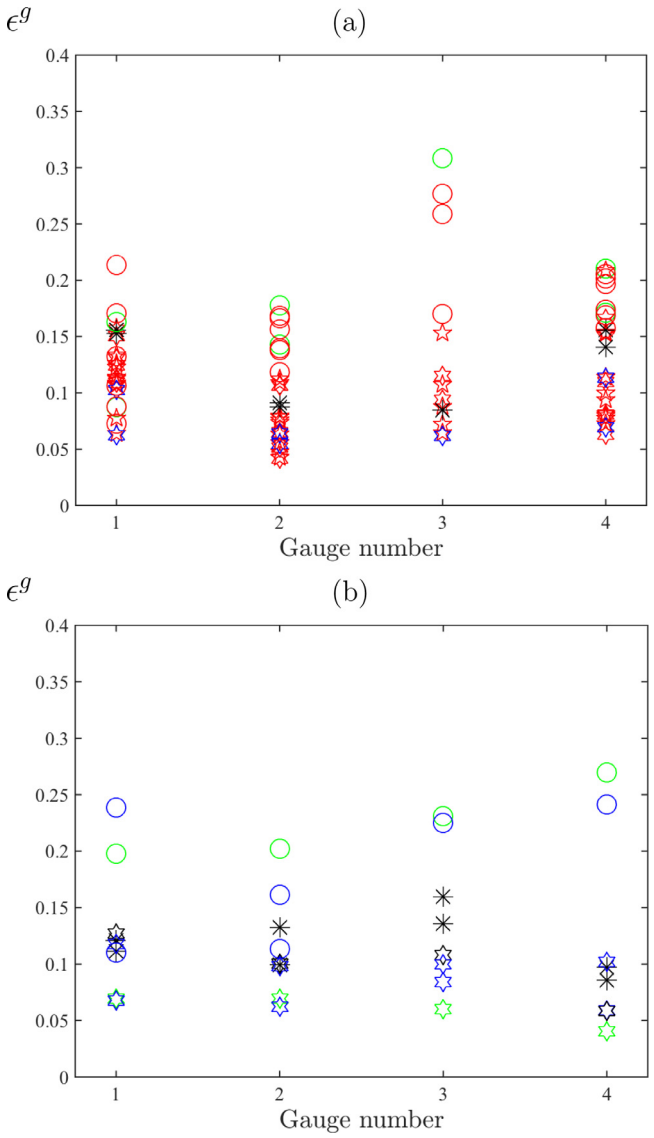

Fig. 13. Distribution of RMS errors ϵ^g for all benchmarked model results (see Table 3 for list, and Fig. 11 caption for symbol definition), by gauge for: (a) Benchmark 2, $d = 61$ mm and 120 mm (Table 2), and (b) Benchmark 4, Test 17. See Fig. 11 caption for symbol definition.

is predicted. Strong biases in total excursion and variance for the hydrostatic models result from their tendency to predict an overly deep wave trough occurring above the moving slide mass. The remaining model types behave consistently, although there is some indication that the Navier–Stokes models are predicting wave packets that are both overly energetic and having too large total surface excursions, compared to the non hydrostatic models, which outperform both of the other two dispersive model categories on these metrics.

5.4. Wavelet analysis of model results

A brief overview of the results of the wavelet analysis of model results detailed in Section 4.2 is provided here, with the bulk of results shown in Appendices D, E and F of Kirby et al. (2018). The results here contrast the non-hydrostatic and hydrostatic versions of NHWAVE, for Benchmark 4 with a granular slide layer; these appear as Models 3 and 16 (Table 3), respectively, in Figs. 11 and 14a, b.

Fig. 15, for the non-hydrostatic case, shows that, with a model that reproduces dispersion properties accurately, the arrival time of energy at distant gauges on a frequency by frequency basis, is correctly predicted. Fig. 15a shows time series of measured and simulated surface elevations at the four gauges WG1–WG4 (Fig. 4); model results are in overall good agreement with the experimental data. In Figs. 15b-e, the modulus $|T|$ of the wavelet transform is plotted as a function of frequency f and time t at each gauge for both the experimental data and model results; again the agreement is overall quite good. In each plot, the thick blue or red lines are drawn through the maxima of the transforms for model and data, respectively, and indicate arrival time for the center of the energy packet at each component frequency or scale in the transform space. The red dashed lines indicate a hypothetical arrival time based on initialization at the time indicated in panel (a) and then being displaced forward in time according to the prediction of linear theory, with later arrival times indicating lower phase speeds with increasing frequency. The deviation of both measured and modeled wave motions could be taken to indicate the tendency for higher frequency components to behave more like bound harmonic of lower frequency components, rather than as free waves, indicating the importance of nonlinearity in the problem. However, as discussed in connection with Fig. 10, the deviation from linear theory prediction is more likely due to the effect of leakage of information across the frequency axis, causing the more energetic lower frequency components to dominate the apparent results at higher frequencies. Overall, the best indicator of proper model performance is a continuing

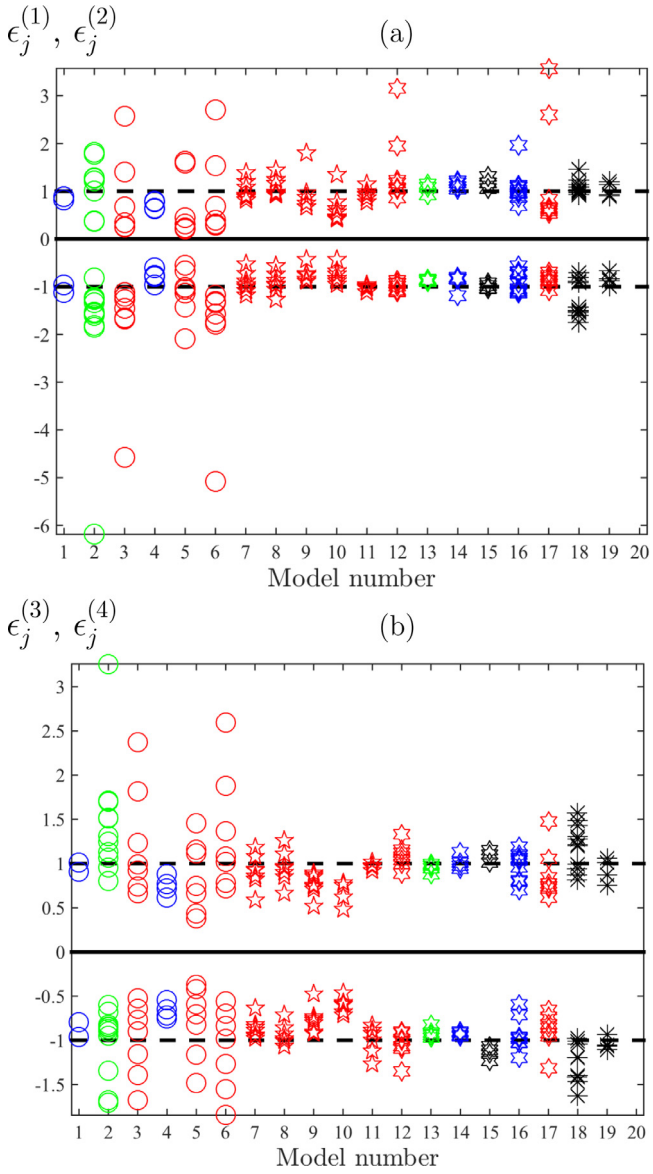

Fig. 14. Normalized surface elevation errors for all benchmarked model results for Benchmarks 2 and 4 at all gauges. See Table 3 for list of model configurations, and Fig. 11 caption for symbol definition. (a) Maximum $\epsilon_j^{(1)}$, plotted as positive values, and $\epsilon_j^{(2)}$, plotted as negative values (Eqs. (13) and (14)); (b) Total surface excursion $\epsilon_j^{(3)}$ (plotted as positive values) and variance $\epsilon_j^{(4)}$ (plotted as negative values) (Eqs. (15) and (16)). Dashed lines at ±1 represent a perfect agreement of model results with the benchmark data.

overlap of the blue and red line segments indicating the arrival of the wave packet maximum.

In contrast, Fig. 16, for the non-dispersive case with Model 16, shows that energy at all frequencies is moving approximately at the same speed as the lower frequency components, which is consistent with the frequency-independent phase speed of $c = \sqrt{gh}$ for all frequencies in this limit. The model results here are strongly contaminated by reflection effects, leading to the double peak in the transform. The lack of any frequency dependence in phase speed is clear, however.

5.5. Benchmark 7: Qualitative analysis

Benchmark 7 differs from Benchmarks 2 and 4 in that there is less basis for a quantitative comparison to observations. In addition, results are subject to choices made by each modeler in setting up the simulation, and thus it is possible that different results could be obtained by different modelers using the same model code. Results were submitted for five models (Table 3): NHWAVE (Model 2), TSUNAMI3D (Model 8), LS3D (Model 12), Alaska GI-L (Model 14) and Landslide-HYSEA (Model 17). Details setup of each model considered may be found in the individual model write-ups at http://www1.udel.edu/kirby/landslide/reporting.html.

We proceed here by showing and discussing the available results for

1. water surface elevation time series at the Navigation Light, Valdez Hotel, P37 and P38 (Fig. 17; Models 2, 8, 12 (partial) 14, 17; Table 3),
2. maximum surface elevation occurring over the Port Valdez domain (Fig. 18; Models 2, 8, 14, 17), and
3. inundation lines in Old Valdez (Fig. 19; Models 2, 8, 12, 14, 17),
4. runups at points identified in Plafker et al. (1969) (Table 4; Models 2, 12).

where the numbers in parentheses indicate models for which the data in question is available.

Time series of surface elevation in Fig. 17a–d, are shown at the Navigation Light, Hotel Valdez and Points 37 and 38 for the results of both slides being superposed, if they were provided separately. Time zero was taken to be the first indication of drawdown above Point 37, which

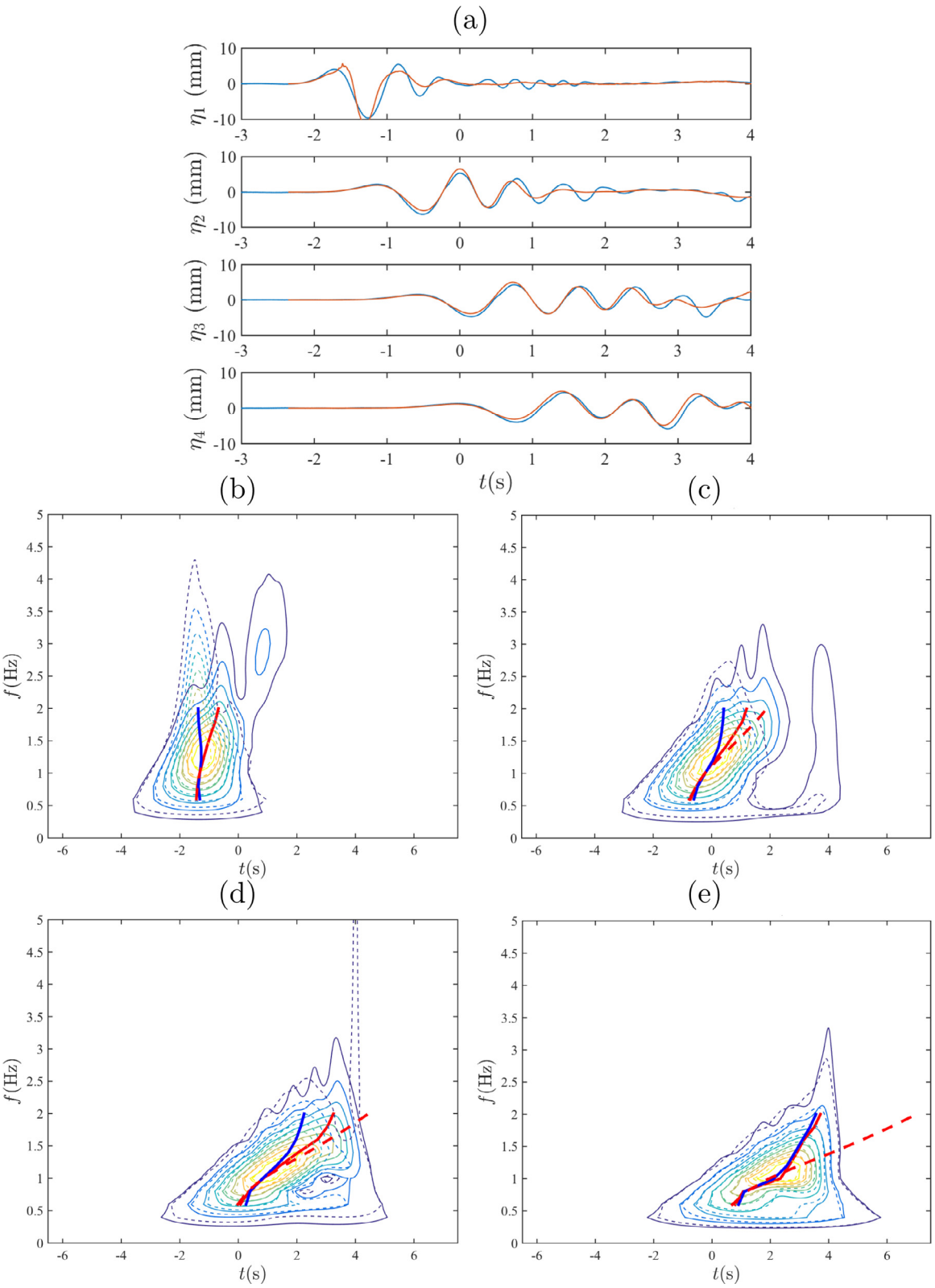

Fig. 15. Wavelet analysis of Benchmark 4. (a) Time series of surface elevation at gauges WG1–WG4 (Fig. 4; top to bottom) for (blue) experimental data, (red) Model 3 results (NHWAVE, granular slide layer, non-hydrostatic). (b-e) Module of wavelet transform $|T|$ computed at gauges WG1–WG4 for: (solid) exp. and (dashed) model; arrival times for each frequency f are shown as thick solid red/blue lines for exp./model, and dashed red lines based on linear (dispersive) theory.

is located over the HPV64 slide in front of Old Valdez (Fig. 8). In the event that results for the two slides were superposed, it was assumed that the start times for each separate slide simulation were the same. The results show interesting patterns of both agreement and difference. At Point 37 (Fig. 17c), where the initial motion is simply the drawdown associated with the HPV64 slide failure, Models 2 and 8, which utilize the same viscous slide model, show nearly the same results up until about 10 min into the simulation, which coincides with the arrival

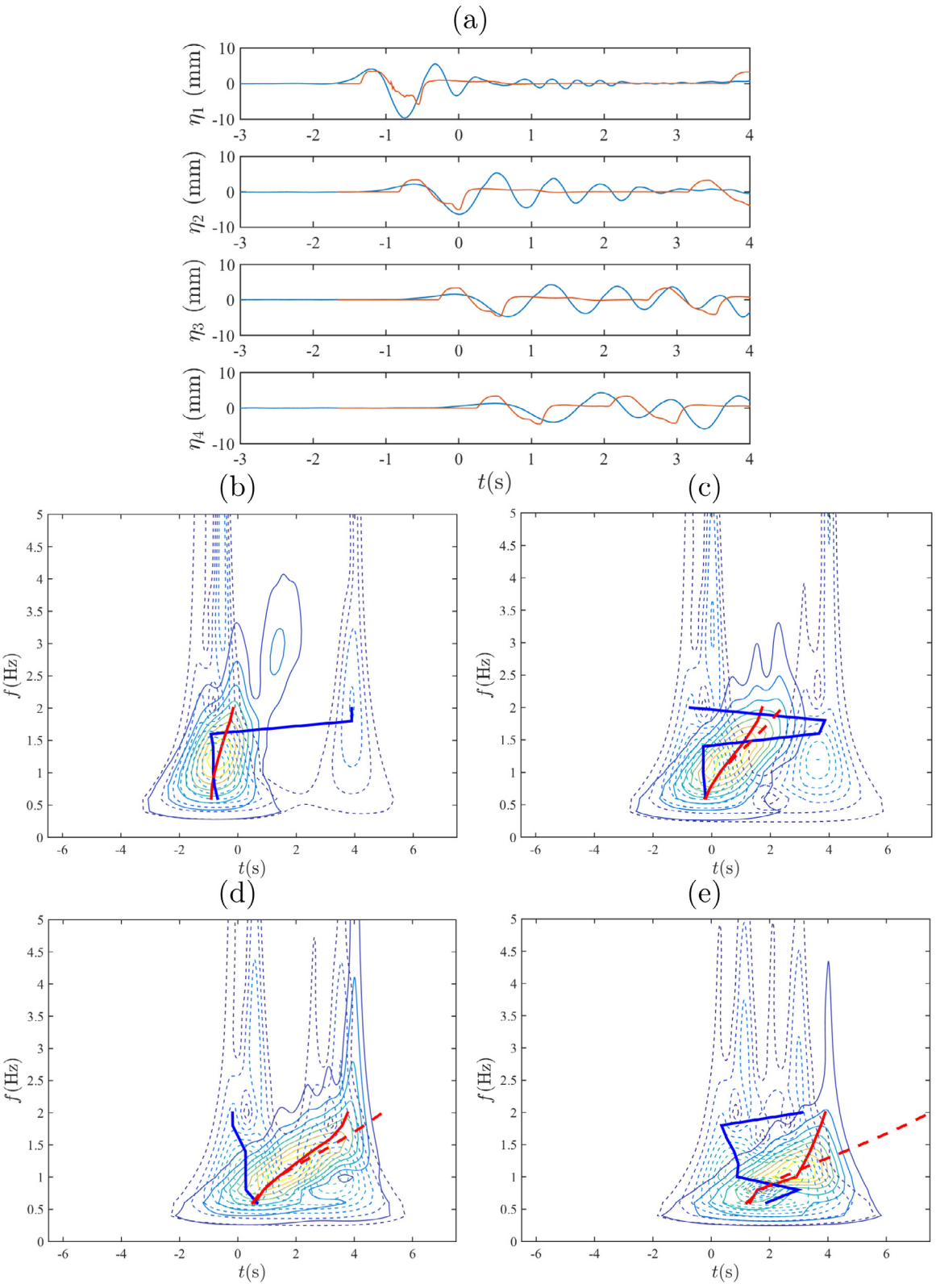

Fig. 16. Same as Fig. 15, but for Model 16 results (NHWAVE, granular slide, hydrostatic).

of the SBM64 (Fig. 8) first wave front. In contrast, the granular slide used in Model 17 shows a drawdown at this location, which is more organized around the time following initial motion, reminiscent of the isolated drawdown at Gauge 1 seen in Benchmark 2 tests. The drawdown predicted by Model 8 (TSUNAMI3D) is more featureless in time and does not show nearly as much higher-frequency structure. Time series for Point 38 (at the Valdez shoreline; Fig. 17d) and the Valdez Hotel (Fig. 7b) show the progression of the first wave resulting from the HPV64 slide, with the wave arriving at Point 38 slightly sooner in Model 14 (hydrostatic) than in Models 2 (non-hydrostatic) and 17 (hydrostatic). Arrival times for the first wave at Hotel Valdez are very consistent and are slightly higher for Model 14 than for Models 2 and 17.

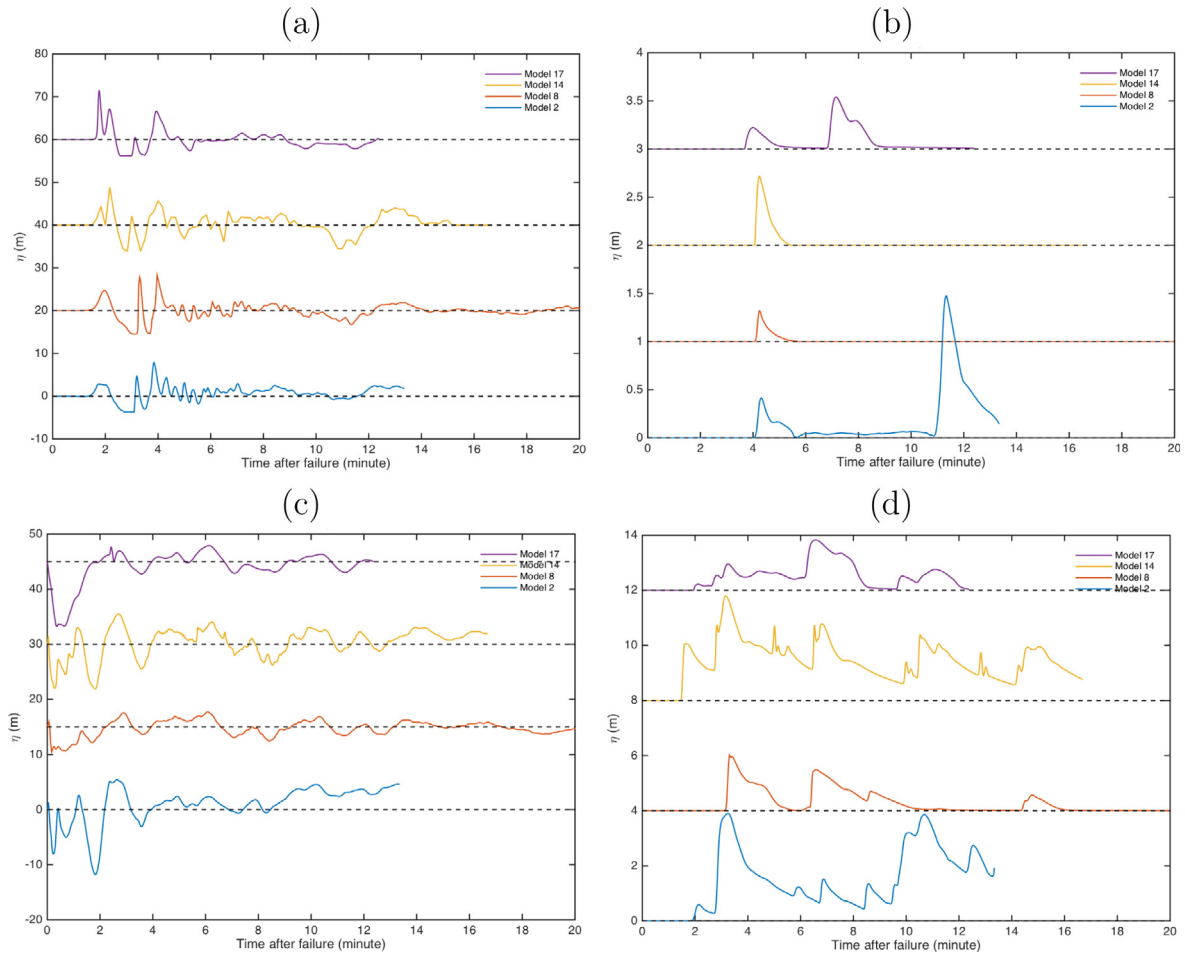

Fig. 17. Simulations of Benchmark 7 with Models 2, 8, 12, 14 and 17 (Table 3). Time series of surface elevation at: (a) the Navigation Light; (b) Hotel Valdez; (c) Point 37; and (d) Point 38.

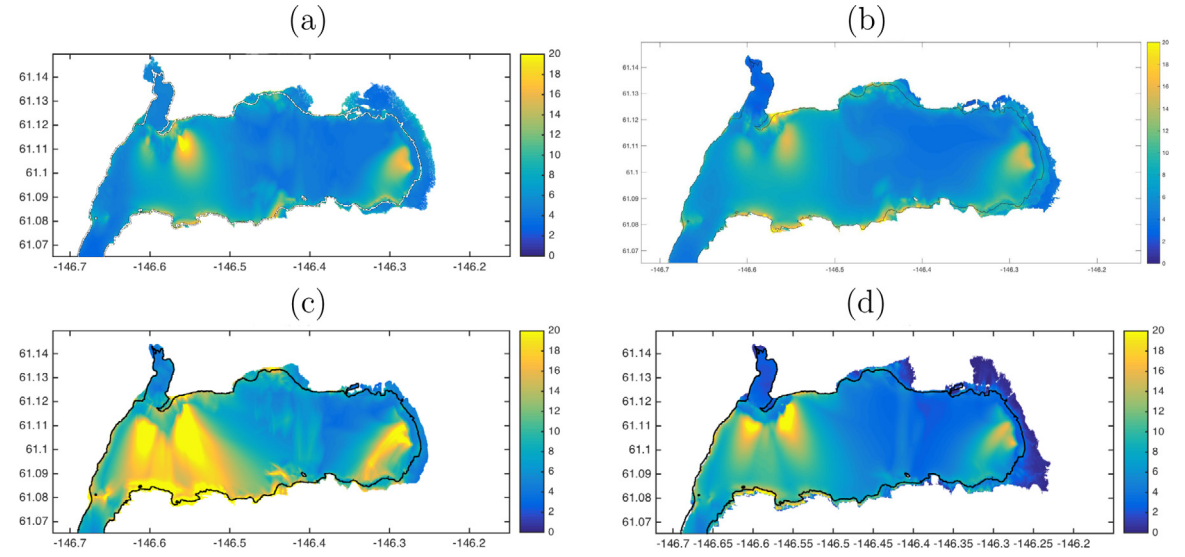

Fig. 18. Simulation of maximum surface elevation over the Port Valdez domain for Benchmark 7, with Model: (a) 2, (b) 8, (c) 14 and (d) 17 (Table 3).

The first arrival at the Navigation Light results from the SBM64 slide in the western portion of the domain. In this case, Models 14 (viscous slide) and 17 (granular slide) give very consistent results for wave height at the Navigation Light, while Model 2 has a very different pattern of arriving waves. A plot of maximum occurring surface elevation over the entire domain in Fig. 18 shows a distinct difference between the results for models 2 and 8, which direct the majority of the SBM64 towards the interior of Port Valdez, and models 14 and 17, which show a much more equal bifurcation of wave direction and an improved simulation of the arrival at the Navigation Light. A

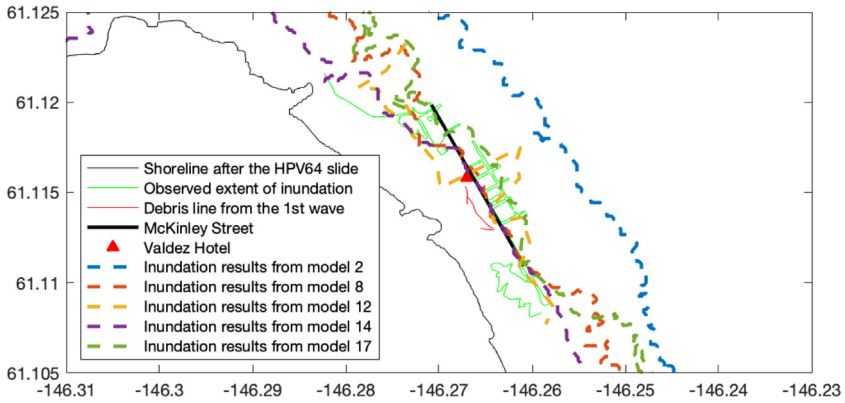

Fig. 19. Simulated inundation lines around Old Valdez for Benchmark 7, with Models 2, 8, 12, 14, 17 (Table 3).

Table 4
Maximum runup at points reported by Plafker et al. (1969).

Lon.°	Lat.°	Plafker (m)	Model 2 (m)	Model 12 (m)
−146.5663	61.1224	51.	33.07	49.28
−146.5947	61.1309	6.	16.73	5.53
−146.6236	61.1168	21.	22.42	24.17
−146.6357	61.1118	37.	35.98	38.32
−146.6759	61.0833	18.	16.14	19.37
−146.6732	61.0786	23.	14.67	19.42
−146.6530	61.0811	11.	7.91	NaN
−146.6443	61.0724	17.	22.80	21.65
−146.6354	61.0758	23.	18.10	21.71
−146.6144	61.0829	10.	15.07	13.29
−146.5989	61.0839	15.	19.90	18.36
−146.5727	61.0777	15.	19.24	12.98
−146.5611	61.0783	20.	22.67	18.30
−146.5428	61.0789	20.	23.36	20.62
−146.5367	61.0793	24.	31.83	24.91
−146.4695	61.0781	12.	22.25	11.26
−146.4594	61.0805	23.	20.67	25.59
−146.4216	61.0850	11.	20.51	12.40
−146.3796	61.0888	9.	11.84	6.34
−146.4453	61.1340	10.	22.98	8.87
−146.4584	61.1339	9.	22.19	10.92
−146.4851	61.1300	18.	20.12	23.77
−146.4959	61.1266	12.	12.95	24.16
−146.5132	61.1232	11.	27.03	17.49
−146.5382	61.1244	27.	44.95	24.99

comparison of predicted maximum runups at observational points listed by Plafker et al. (1969) with observed results are shown in Table 4, and also show the overprediction by model 2 at sites within Port Valdez.

The tendency for model 2 to direct the majority of the simulated wave energy to the interior of Port Valdez led to an over-prediction of the extent of tsunami inundation in the area of Old Valdez, shown previously in Fig. 17(b) for Hotel Valdez and (d) for point 38, closer to the Old Valdez waterfront. The overly large second wave leads to an overprediction of the extent of inundation around Old Valdez, in comparison to observations and other model results, which are more consistent (Fig. 19). The reason for these anomalies has not been further examined.

6. Discussion and conclusions

A landslide tsunami model benchmarking workshop was organized in 2017 on behalf of the US National Tsunami Hazard Mitigation (NTHMP) program (see https://nws.weather.gov/nthmp/2017MMSLandslide/index.html), with the goals to evaluate the state of numerical models for the prediction of tsunamis generated by subaerial or submarine landslides (or, more generally, submarine mass failures; SMFs) and draw recommendations for best practice in model selection and modeling of these events. Nine landslide tsunami models, with 20 different model configurations tested (Table 3) were submitted for benchmarking, which were regrouped into 4 classes representing : (1) hydrostatic models with no frequency dispersion; (2) Boussinesq or one-layer weakly dispersive models (essentially a two-dimensional (2D) horizontal framework); (3) Multi-layer or non-hydrostatic (i.e., dispersive) models (three-dimensional (3D) framework but with a limited discretization in the vertical direction); and (4) Full 3D Navier–Stokes models.

Seven benchmarks were proposed to the participants, 6 based on published laboratory experiments and one being the historical case study of 1964 Port Valdez, Alaska, but modelers were only requested to simulate Benchmarks 2, 4 and 7, with 2 and 4 being laboratory experiments for a solid and granular slide, respectively, and 7 being the Port Valdez case study. Results and a comparison of model performance on these 3 benchmarks were presented in this paper. Results presented here show that overall, models that included non-hydrostatic (i.e., dispersive) effects, whether solving the full Navier–Stokes, Euler, or long wave Boussinesq type equations (classes 2–4), performed much better on a variety of error metrics than non-dispersive (hydrostatic)

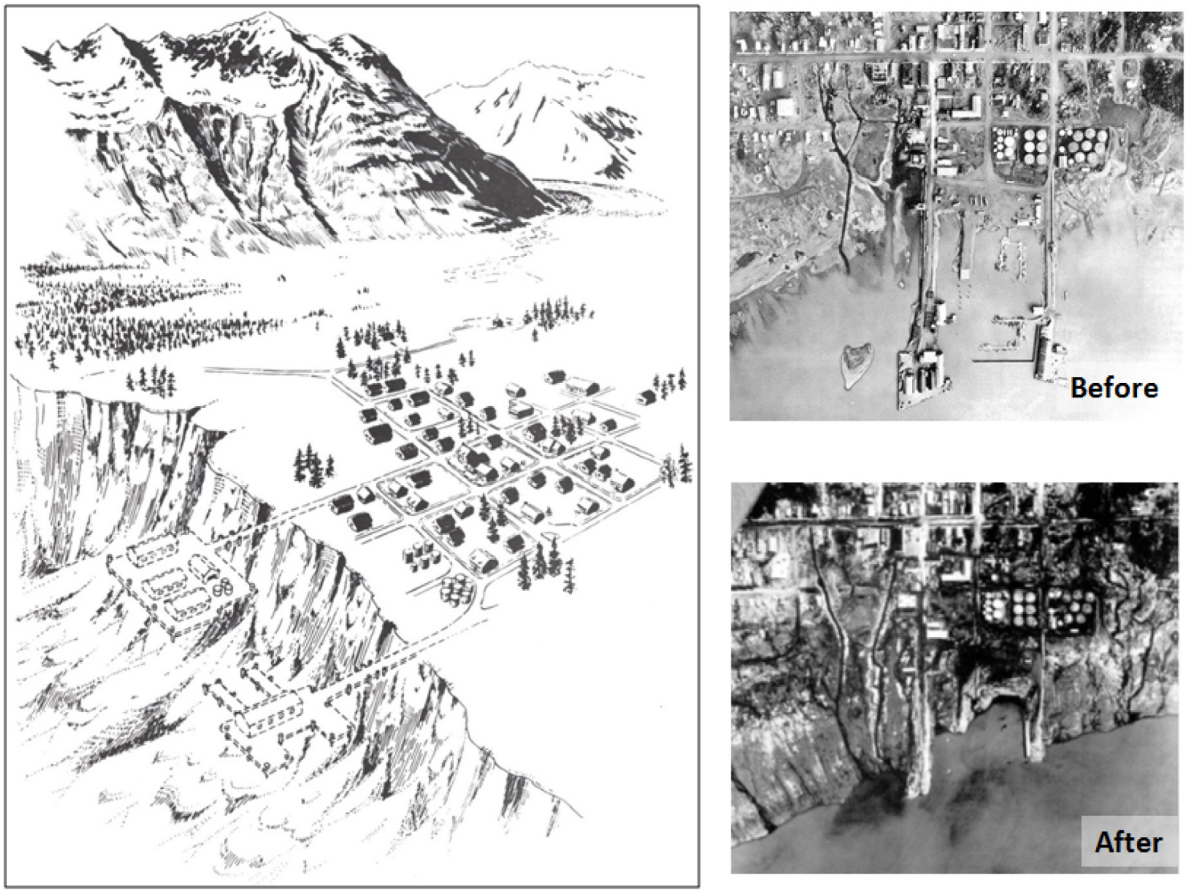

Fig. B.1. Oblique view of slide area at Valdez. Dashed lines indicate dock area destroyed in earthquake. Aerial photographs show the waterfront area of old Valdez before and after the tsunami event (Coulter and Migliaccio, 1966).

models (class 1). The latter include standard tsunami models based on the nonlinear shallow water equations widely applied to coseismic tsunamis. Hydrostatic models fail by a large margin to reproduce benchmark data in most cases, particularly when significant dispersive effects are present.

On this basis, whenever possible, it is recommended using a dispersive model for landslide tsunami modeling. If dispersion effects matter for tsunami processes occurring in a particular application, the physics included in the model will accurately simulate these effects. In contrast, if dispersion does not matter in the application, likewise, no strong dispersive effects will occur in results of a dispersive model, which will nevertheless be accurate since non-dispersive problems can also be solved in dispersive models. More detailed recommendations and guidance have been prepared for NTHMP modelers and can be found in NTHMP guidelines established on the basis of the workshop (see https://nws.weather.gov/nthmp/mapping_subcommittee.html).

Several workshop participants have provided separate documentation of model performance for a partial or complete set of the workshop benchmarks in journal publications or technical reports. Zhang et al. (2017) provide results or the full set of seven benchmarks, using various configurations of NHWAVE, while Macías et al. (2021a) and Macías et al. (2021b) have provided documentation for benchmarks 1–6.

CRediT authorship contribution statement

James T. Kirby: Conception and design of study, Analysis and/or interpretation of data, Writing – original draft. **Stephan T. Grilli:** Conception and design of study, Analysis and/or interpretation of data, Writing – original draft. **Juan Horrillo:** Conception and design of study, Acquisition of data, Writing – review & editing. **Philip L.-F. Liu:** Conception and design of study, Writing – review & editing. **Dmitry Nicolsky:** Conception and design of study, Acquisition of data, Writing – original draft. **Stephane Abadie:** Acquisition of data, Writing – review & editing. **Behzad Ataie-Ashtiani:** Acquisition of data, Writing – review & editing. **Manuel J. Castro:** Acquisition of data, Writing – review & editing. **Lucie Clous:** Acquisition of data, Writing – review & editing. **Cipriano Escalante:** Acquisition of data, Writing – review & editing. **Isaac Fine:** Acquisition of data, Writing – review & editing. **José Manuel González-Vida:** Acquisition of data, Writing – review & editing. **Finn Løvholt:** Acquisition of data, Writing – review & editing. **Patrick Lynett:** Acquisition of data, Writing – review & editing. **Gangfeng Ma:** Acquisition of data, Writing – review & editing. **Jorge Macías:** Acquisition of data, Writing – review & editing. **Sergio Ortega:** Acquisition of data, Writing – review & editing. **Fengyan Shi:** Acquisition of data, Writing – review & editing. **Saeedeh Yavari-Ramshe:** Acquisition of data, Writing – review & editing. **Cheng Zhang:** Acquisition of data, Writing – review & editing.

Declaration of competing interest

The authors declare that they have no known competing financial interests or personal relationships that could have appeared to influence the work reported in this paper.

Acknowledgments

The benchmark workshop and development of documentation and NTHMP modeling guidelines was supported by NOAA, USA grants NA15-NWS4670029, NA16-NWS4670034, and NA17-NWS4670010 to the University of Delaware and NA18-NWS4670073 to NESEC, USA. Kirby, Grilli, Ma, Shi and Zhang were supported by National Science

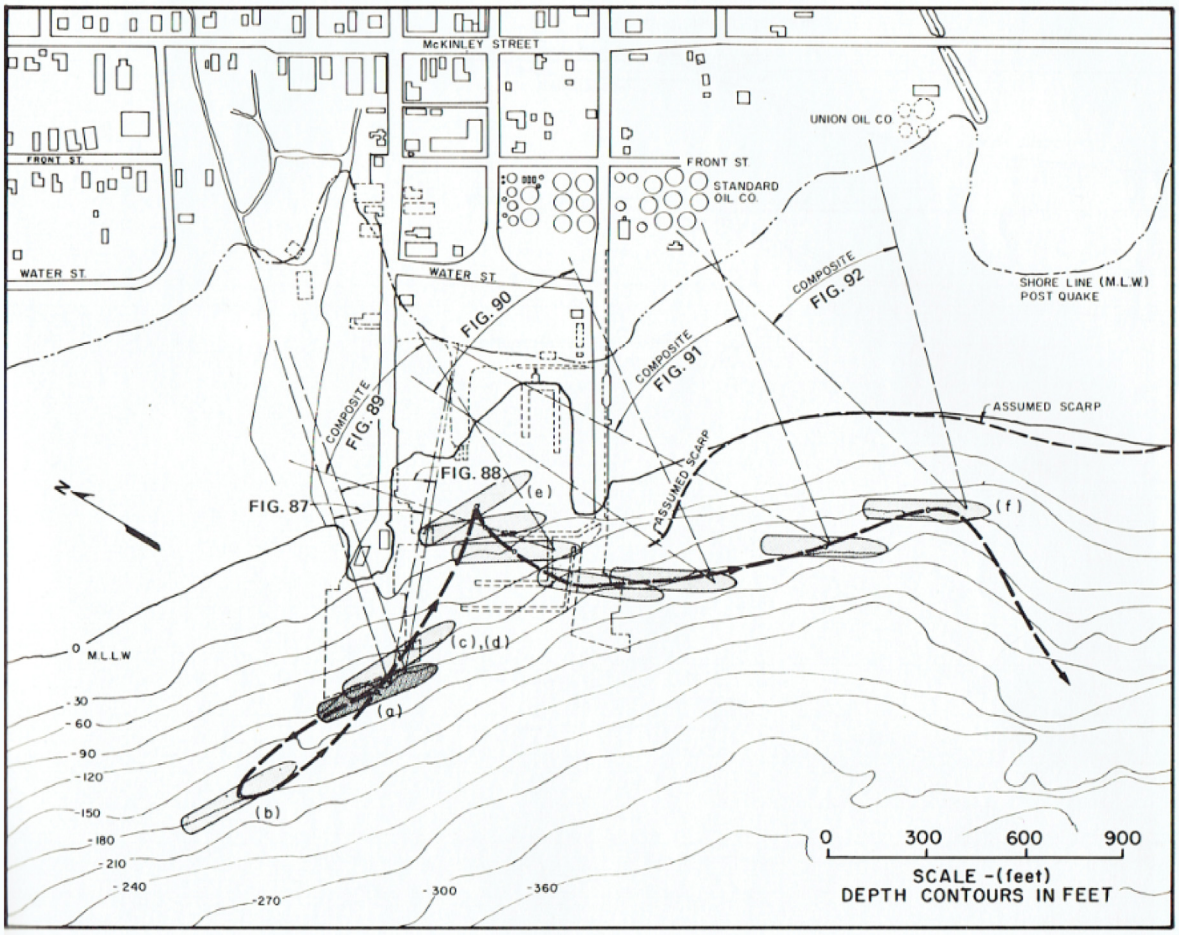

Fig. B.2. Inferred path of the *Chena* from its initial position at the dock during the earthquake (Wilson and Torum, 1972).

Foundation, USA grants CMMI-1537568, -1537232 and -1537100 to the Universities of Rhode Island and Delaware and to Old Dominion University. PLF Liu would like to acknowledge the support through a grant to National University of Singapore from the National Research Foundation (NRF2018NRF-NSFC003ES-002) and the Yushan Scholar Program Award from the Ministry of Education in Taiwan. Pat Lynett acknowledges support from the California Geological Survey and the National Science Foundation, USA (CMMI-1661052). Macías, Escalante, Castro, González-Vida and Ortega acknowledge the support of the Spanish Government FEDER project MEGAFLOW (Grant RTI2018-096064-B-C21). Abadie and Clous acknowledge the support of the ANR, France project RAVEX (Grant ANR-16-CE03-0002) All model results presented in this study may be obtained from http://www1.udel.edu/kirby/landslide/reporting.html

Approval of the version of the manuscript to be published (the names of all authors must be listed): J. T. Kirby, S. T. Grilli, J. Horillo, P. L.-F. Liu, D. Nicolsky, S. Abadie, B. Ataie-Ashtiani, M. J. Castro, L. Clous, C. Escalante, I. Fine, J. M. Gonzalez-Vida, F. Lovholt, P. Lynett, G. Ma, J. Macias, S. Ortega, F. Shi, S. Yavari-Ramshe, C. Zhang.

Appendix A. The continuous wavelet transform (CWT)

To illustrate the ideas behind the CWT, consider 'sampling' some function $f(t)$ using a window $w(t-\tau)$, where the lag τ centers the observing window on the time axis. The resulting sample is a function both of time and the location of the sample window,

$$g(t,\tau) = f(t)w(t-\tau) \tag{A.1}$$

This operation provides localization in time for the sample. This function may then be Fourier transformed to obtain

$$\hat{g}(\omega,\tau) = \frac{1}{2\pi}\int_{-\infty}^{\infty} g(t,\tau)\mathrm{e}^{-i\omega t}dt = \frac{1}{2\pi}\int_{-\infty}^{\infty} f(t)w(t-\tau)\mathrm{e}^{-i\omega t}dt \tag{A.2}$$

The resulting transform $\hat{g}$ then provides information about the signal that is localized in frequency as well as time. Consider the typical case of sampling the signal with a unit amplitude window of length T, or

$$w(t-\tau) = \begin{cases} 0 & |\, t-\tau\,| > T/2 \\ 1 & |\, t-\tau\,| \le T/2 \end{cases} \tag{A.3}$$

This leads to the result

$$\hat{g}_T(\omega,\tau) = \frac{1}{2\pi}\int_{\tau-T/2}^{\tau+T/2} f(t)\mathrm{e}^{-i\omega t}dt \tag{A.4}$$

the usual windowed Fourier Transform. For relatively small T's, this process may be thought of as a means of localizing transform information in time, but the general result has some undesirable properties. First, frequency resolution $\Delta\omega$ is controlled by the sample length T, and the only means for improving frequency resolution is to increase T and thus lose temporal localization. The converse is true, and the result is that the product $T\Delta\omega$ is a constant, with T and $\Delta\omega$ individually constant over the entire transform space (ω,τ). The constancy of the product is a consequence of a result analogous to the Heisenberg Uncertainty Principle limiting the combined uncertainty of knowledge of a particle's position and speed in quantum mechanics. This result cannot be circumvented in a given sampling procedure. However, steps can be taken to adaptively change frequency or temporal resolution in a

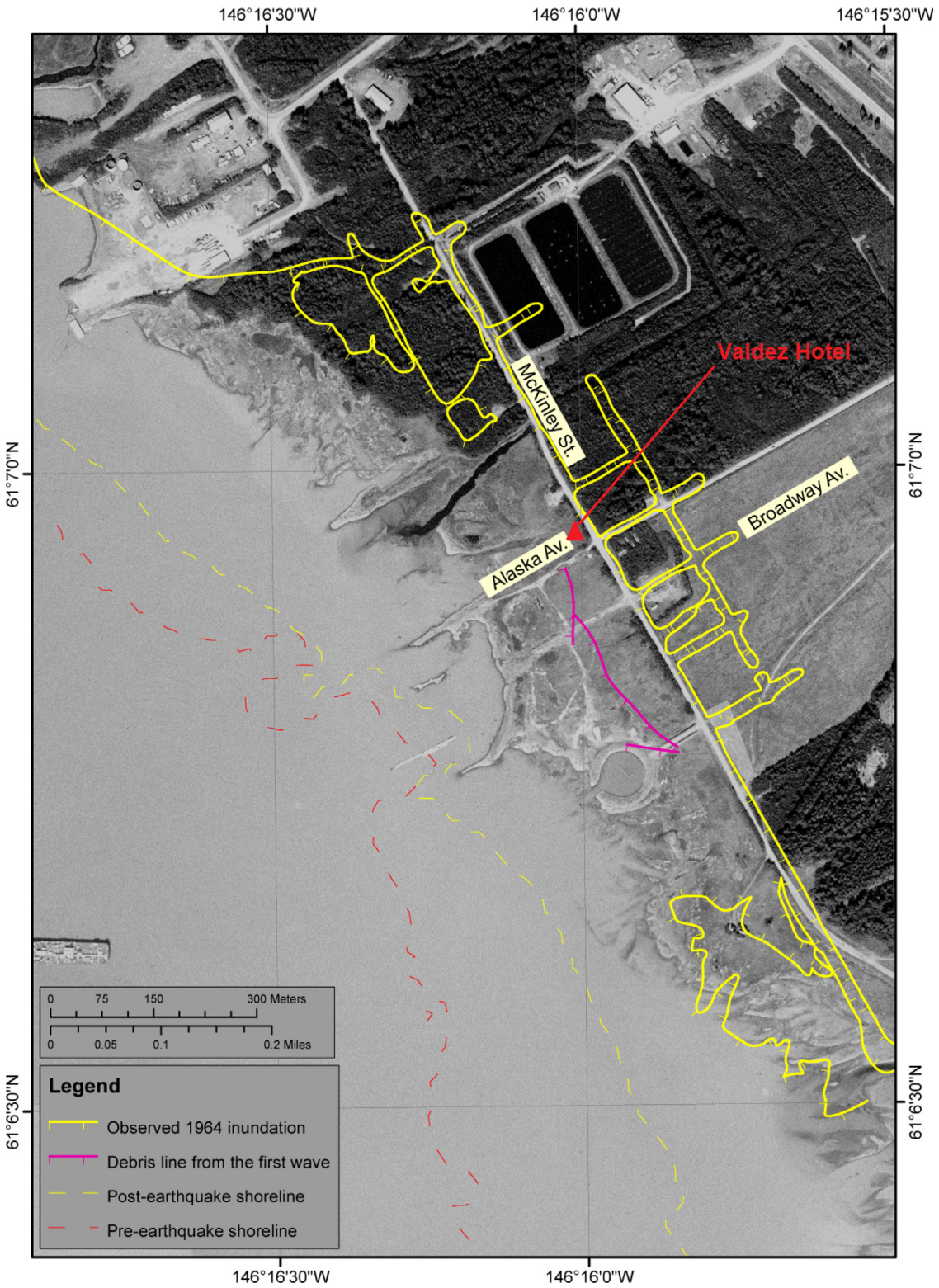

Fig. B.3. Aerial view of old town. The yellow line represents the limit of observed inundation caused by both landslide tsunamis. Water flow was channeled along streets due to high snow berms, which are not represented in the supplied model DEMs. Hachures indicate the water side of the inundation lines (Nicolsky et al., 2013).

manner that sacrifices frequency resolution at high frequencies (where the signal varies rapidly) in order to obtain better time localization, or to sacrifice time localization in slowly varying portions of the signal in order to improve frequency discrimination. The CWT is a popular tool for carrying this out. The CWT is usually defined as a function of lag τ and a scale a, where a may be roughly thought of as being the inverse of a frequency. We define the transform here as

$$T(\tau, a) = \frac{1}{\sqrt{a}} \int_{-\infty}^{\infty} w^* \left(\frac{t-\tau}{a} \right) dt \tag{A.5}$$

where $w((t-\tau)/a)$ is referred to as the 'analyzing wavelet', and varies in duration as a function of the scale a being analyzed. A relation between scale and frequency may be established by examining the

Fourier transform pair

$$\hat{f}(\omega) = F(f(t)) = \frac{1}{2\pi}\int_{-\infty}^{\infty} f(t)\mathrm{e}^{-i\omega t}dt$$
$$f(t) = F^{-1}(\hat{f}(\omega)) = \int_{-\infty}^{\infty} \hat{f}(\omega)\mathrm{e}^{i\omega t} \quad (A.6)$$

The transform of $f(t/a)$ then works out directly to

$$F(f(t/a)) = a\hat{f}(\omega a) \quad (A.7)$$

so that compressing time by a factor a amounts to multiplying frequency by that factor.

Here, we use a common choice for the analyzing wavelet given by the Morlet wavelet

$$w(t/a) = \mathrm{e}^{i(t/a)-(t/a)^2/2} = \mathrm{e}^{i\omega_0 t-(\omega_0 t)^2/2} \quad (A.8)$$

where $\omega_0 = 1/a$ is a chosen reference frequency which essentially determines the number of oscillations occurring within the wavelet's Gaussian envelope. The Fourier Transform of $w(t/a)$ is then given to a very good approximation by

$$\hat{w}(\omega a) = \mathrm{e}^{-(\omega a-\omega_0)^2} \quad (A.9)$$

The transform is usually computed conveniently in Fourier space, rather than calculating the convolution integral in the time domain. An overview of the basic computational approach may be found in Torrence and Campo (1998).

Appendix B. Informational plots for Benchmark 7 background

See Figs. B.1–B.3.

References

Abadie, S., Harris, J.C., Grilli, S.T., Fabre, R., 2012. Numerical modeling of tsunami waves generated by the flank collapse of the Cumbre Vieja Volcano (La Palma, Canary Islands): Tsunami source and near field effects. J. Geophys. Res. 117, C05030. http://dx.doi.org/10.1029/2011JC007646.

Abadie, S., Morichon, D., Grilli, S., Glockner, S., 2010. Numerical simulation of waves generated by landslides using a multiple-fluid Navier-stokes model. Coast. Eng. 57 (9), 779–794. http://dx.doi.org/10.1016/j.coastaleng.2010.03.003.

Addison, P.S., 2018. Introduction to redundancy rules: the continuous wavelet transform comes of age. Phil. Trans. R. Soc. A 376, 20170258. http://dx.doi.org/10.1098/rsta.2017.0258.

Assier-Rzadkiewicz, S., Mariotti, C., Heinrich, P., 1997. Numerical simulation of submarine landslides and their hydraulic effects. J. Waterw. Port Coast. Ocean Eng. 123 (6), 149–157.

Ataie-Ashtiani, B., Najafi-Jilani, A., 2007. A higher order Boussinesq-type model with moving bottom boundary: applications to submarine landslide tsunami waves. Internat. J. Numer. Methods Fluids 53, 1019–1048. http://dx.doi.org/10.1002/fld.1354.

Ataie-Ashtiani, B., Najafi-Jilani, A., 2008. Laboratory investigations on impulsive waves caused by underwater landslide. Coast. Eng. 55 (12), 989–1004. http://dx.doi.org/10.1016/j.coastaleng.2008.03.003.

Ataie-Ashtiani, B., Nik-khah, A., 2008. Impulsive waves caused by subaerial landslides. Environ. Fluid Mech. 8 (3), 263–280. http://dx.doi.org/10.1007/s10652-008-9074-7.

Ataie-Ashtiani, B., Shobeyri, G., 2008. Numerical simulation of landslide impulsive waves by incompressible smoothed particle hydrodynamics. Internat. J. Numer. Methods Fluids 56 (2), 209–232. http://dx.doi.org/10.1002/fld.1526.

Atlantic and Gulf of Mexico Tsunami Hazard Assessment Group, 2008. Evaluation of tsunami sources with the potential to impact the U.S. Atlantic and Gulf Coasts - a report to the Nuclear Regulatory Commission. Administrative Report, U. S. Geological Survey.

Bai, Y., Cheung, K.F., 2013. Dispersion and nonlinearity of multi-layer non-hydrostatic free-surface flow. J. Fluid Mech. 726, 226–260. http://dx.doi.org/10.1017/jfm.2013.213.

Bellotti, G., Cecioni, C., De Girolamo, P., 2008. Simulation of small-amplitude frequency-dispersive transient waves by means of the mild-slope equation. Coast. Eng. 55, 447–458. http://dx.doi.org/10.1016/j.coastaleng.2007.12.006.

Berkhoff, J.C.W., 1972. Computation of combined refraction-diffraction. In: Proceedings of the XX International Conference on Coastal Engineering. ASCE, Vancouver, pp. 471–490.

ten Brink, U.S., Chaytor, J.D., Geist, E.L., Brothers, D.S., Andrews, B.D., 2014. Assessment of tsunami hazard to the U. S. Atlantic margin. Mar. Geol. 353, 31–54. http://dx.doi.org/10.1016/j.margeo.2014.02.011.

Brocchini, M., 2013. A reasoned overview on Boussinesq-type models: the interplay between physics, mathematics and numerics. Proc. R. Soc. Lond. Ser. A Math. Phys. Eng. Sci. 469 (2160), 20130496. http://dx.doi.org/10.1098/rspa.2013.0496.

Chaytor, J.D., Geist, E.L., Paull, C.K., Caress, D.W., Gwiazda, R., Urrutia Fucugauchi, R., Rebolledo Vieyra, M., 2016. Source characterization and tsunami modeling of submarine landslides along the Yucatán Shelf/Campeche Escarpment, southern Gulf of Mexico. Pure Appl. Geophys. 173 (12), 4101–4116. http://dx.doi.org/10.1007/s00024-016-1363-3.

Clous, L., Abadie, S., 2019. Simulation of energy transfers in waves generated by granular slides. Landslides 16 (9), 1663–1679.

Coulter, H.W., Migliaccio, R.R., 1966. Effects of the earthquake of March 27, 1964 at Valdez, Alaska. Geological Survey Professional Pape 542-C, United States Dept. of Interior - Geological Survey.

Day, S.J., Watts, P., Grilli, S.T., Kirby, J.T., 2005. Mechanical models of the 1975 kalapana, hawaii earthquake and tsunami. Mar. Geol. 215 (1–2), 59–92. http://dx.doi.org/10.1016/j.margeo.2004.11.008.

Enet, F., Grilli, S.T., 2007. Experimental study of tsunami generation by three-dimensional rigid underwater landslides. J. Waterw. Port Coast. Ocean Eng. 133 (6), 442–454. http://dx.doi.org/10.1061/(ASCE)0733-950X(2007)133:6(442).

Fine, I., Rabinovich, A., Bornhold, B., Thomson, R., Kulikov, E., 2005. The grand banks landslide-generated tsunami of november 18, 1929: Preliminary analysis and numerical modeling. Mar. Geol. 215, 45–57. http://dx.doi.org/10.1016/j.margeol.2004.11.007.

Fine, I.V., Rabinovich, A.B., Kulikov, E.A., 1998. Numerical modelling of landslide generated tsunamis with application to the Skagway Harbor tsunami of November 3, 1994. In: Proc. Intl. Conf. on Tsunamis, Paris, pp. 211–223.

Fritz, H., Hager, W., Minor, H.-E., 2001. Lituya Bay case: Rockslide impact and wave run-up. Sci. Tsunami Hazards 19, 3–22.

Fritz, H.M., Hager, W.H., Minor, H.-E., 2004. Near-field characteristics of landslide generated impulse waves. J. Waterw. Port Coast. Ocean Eng. 130, 287–302. http://dx.doi.org/10.1061/(ASCE)0733-950X(2004)130:6(287).

Fritz, H.M., Mohammed, F., Yoo, J., 2009. Lituya bay landslide impact generated mega-tsunami 50th anniversary. Pure Appl. Geophys. 166, 153–175. http://dx.doi.org/10.1007/s00024-008-0435-4.

Geist, E., Lynett, P., Chaytor, J., 2009. Hydrodynamic modeling of tsunamis from the Currituck landslide. Mar. Geol. 264, 41–52. http://dx.doi.org/10.1016/j.margeo.2008.09.005.

George, D.L., Iverson, R.M., 2011. A two-phase debris-flow model that includes coupled evolution of volume fractions, granular dilatancy, and pore-fluid pressure. Ital. J. Eng. Geol. Environ. 43, 415–424. http://dx.doi.org/10.4408/IJEGE.2011-03.B-047.

George, D.L., Iverson, R.M., 2014. A depth-averaged debris-flow model that includes the effects of evolving dilatancy. II. Numerical predictions and experimental tests. Proc. R. Soc. Lond. Ser. A Math. Phys. Eng. Sci. 470 (2170), 20130820. http://dx.doi.org/10.1098/rspa.2013.0820.

Glimsdal, S., Pedersen, G., Harbitz, C., Lø vholt, F., 2013. Dispersion of tsunamis: does it really matter? Nat. Hazards Earth Syst. Sci. 13, 1507–1526. http://dx.doi.org/10.5194/nhess-13-1507-2013.

González-Vida, J.M., Macías, J., Castro, M.J., Sánchez-Linares, M., Ortega-Acosta, S., Arcas, D., 2019. The lituya bay landslide-generated mega-tsunami. Numerical simulation and sensitivity analysis. Nat. Hazards Earth Syst. Sci. 19, 369–388. http://dx.doi.org/10.5194/nhess-19-369-2019.

Greene, H., Murai, L., Watts, P., Maher, N., Fisher, M.A., Paull, C., Eichhubl, P., 2005. Submarine landslides in the Santa Barbara Channel as potential tsunami sources. Nat. Hazards Earth Syst. Sci. 6 (1), 63–88.

Greene, H., Ward, S., 2003. Mass movement features along the central California margin and their modeled consequences for tsunami generation. In: Submarine Mass Movements and their Consequences. Springer Netherlands, pp. 343–356.

Grilli, S.T., Dias, F., Guyenne, P., Fochesato, C., Enet, F., 2010. Progress in fully nonlinear potential flow modeling of 3D extreme ocean waves. In: Advances in Numerical Simulation of Nonlinear Water Waves. World Scientific, pp. 75–128.

Grilli, S.T., O'Reilly, C., Harris, J.C., Tajalli-Bakhsh, T., Tehranirad, B., Banihashemi, S., Kirby, J.T., Baxter, C.D.P., Eggeling, T., Ma, G., Shi, F., 2015. Modeling of SMF tsunami hazard along the upper US East Coast: Detailed impact around ocean city, MD. Nat. Hazards 76 (2), 705–746. http://dx.doi.org/10.1007/s11069-014-1522-8.

Grilli, S.T., Shelby, M., Kimmoun, O., Dupont, G., Nicolsky, D., Ma, G., Kirby, J.T., Shi, F., 2017. Modeling coastal tsunami hazard from submarine mass failures: effect of slide rheology, experimental validation, and case studies off the U S East Coast. Nat. Hazards 86, 353–391. http://dx.doi.org/10.1007/s11069-016-2692-3.

Grilli, S.T., Tappin, D.R., Carey, S., Watt, S.F.L., Ward, S.N., Grilli, A.R., Engwell, S.L., Zhang, C., Kirby, J.T., Schambach, L., Muin, M., 2019. Modelling of the tsunami from the december 22, 2018 lateral collapse of anak krakatau volcano in the sunda straits, Indonesia. Sci. Rep. 9 (1), 1–13. http://dx.doi.org/10.1038/s41598-019-48327-6.

Grilli, S.T., Taylor, O.-D.S., Baxter, C.D., Maretzki, S., 2009. Probabilistic approach for determining submarine landslide tsunami hazard along the upper East Coast of the United States. Mar. Geol. 264 (1–2), 74–97. http://dx.doi.org/10.1016/j.margeo.2009.02.010.

Grilli, S.T., Vogelmann, S., Watts, P., 2002. Development of a 3D numerical wave tank for modeling tsunami generation by underwater landslides. Eng. Anal. Bound. Elem. 26 (4), 301–313.

Grilli, S.T., Watts, P., 1999. Modeling of waves generated by a moving submerged body. Applications to underwater landslides. Eng. Anal. Bound. Elem. 23, 645–656.

Grilli, S.T., Watts, P., 2005. Tsunami generation by submarine mass failure. I: Modeling, experimental validation, and sensitivity analysis. J. Waterw. Port Coast. Ocean Eng. 131 (6), 283–297. http://dx.doi.org/10.1061/(ASCE)0733-950X(2005)131:6(283).

Grilli, S.T., Zhang, C., Kirby, J.T., Grilli, A.R., Tappin, D.R., Watt, S.F.L., Hunt, J.E., Novellino, A., Engwell, S., Nurshal, M.E.M., Abdurrachman, M., Cassidy, M., Madden-Nadeau, L., Day, S., 2021. Modeling of the Dec. 22nd 2018 Anak Krakatau volcano lateral collapse and tsunami based on recent field surveys: Comparison with observed tsunami impact. Mar. Geol. 440, 106566. http://dx.doi.org/10.1016/j.margeo.2021.106566.

Gylfadóttir, S.S., Kim, J., Helgason, J.K., Brynjólfsson, S., Hóskuldsson, A., Jóhannesson, T., Harbitz, C.B., Lovholt, F., 2017. The 2014 Lake Askja rockslide-induced tsunami: Optimization of numerical tsunami model using observed data. J. Geophys. Res. Oceans 122, 4110–4122. http://dx.doi.org/10.1002/2016JC012496.

Harbitz, C.B., Løvholt, F., Bungum, H., 2014. Submarine landslide tsunamis: how extreme and how likely? Nat. Hazards 72 (3), 1341–1374.

Harbitz, C., Pedersen, G., Gjevik, B., 1993. Numerical simulations of large water waves due to landslides. J. Hydraul. Eng. 119, 1325–1342.

Heidarzadeh, M., Satake, K., 2015. Source properties of the 17 July 1998 Papua New Guinea tsunami based on tide gauge records. Geophys. J. Int. 202 (1), 361–369.

Heinrich, P., 1992. Nonlinear water waves generated by submarine and aerial landslides. J. Waterw. Port Coast. Ocean Eng. 118, 249–266.

Heller, V., Hager, W.H., 2010. Impulse product parameter in landslide generated impulse waves. J. Waterw. Port Coast. Ocean Eng. 136, 145–155. http://dx.doi.org/10.1061/(ASCE)WW.1943-5460.0000037.

Higman, B., Shugar, D.H., Stark, C.P., Ekström, G., Koppes, M.N., Lynett, P., Dufresne, A., Haeussler, P.J., Geertsema, M., Gulick, S., et al., 2018. The 2015 landslide and tsunami in Taan Fiord, Alaska. Sci. Rep. 8 (1), 1–12.

Horrillo, J., Grilli, S., Nicolsky, D., Roeber, V., Zhang, J., 2014. Performance benchmarking tsunami operational models for NTHMP's inundation mapping activities. Pure Appl. Geophys. 172, 869–884. http://dx.doi.org/10.1007/s00024-014-0891-y.

Horrillo, J., Wood, A., Kim, G.-B., Parambath, A., 2013. A simplified 3-D Navier-Stokes numerical model for landslide-tsunami: Application to the Gulf of Mexico. J. Geophys. Res. Oceans 118, 6934–6950. http://dx.doi.org/10.1002/2012JC008689.

Ichinose, G., Somerville, P., Thio, H., Graves, R., O'Connell, D., 2007. Rupture process of the 1964 Prince William Sound, Alaska, earthquake from the combined inversion of seismic, tsunami, and geodetic data. J. Geophys. Res. 112, B07306. http://dx.doi.org/10.1029/2006JB004728.

Jiang, L., LeBlond, P.H., 1992. The coupling of a submarine slide and the surface waves which it generates. J. Geophys. Res. 97 (C8), 12731–12744.

Jiang, L., LeBlond, P.H., 1993. Numerical modeling of an underwater Bingham plastic mudslide and the waves which it generates. J. Geophys. Res. 98 (C6), 10303–10317.

Jiang, L., LeBlond, P.H., 1994. Three-dimensional modeling of tsunami generation due to a submarine mudslide. J. Phys. Oceanogr. 24, 559–572.

Kim, J., Lovholt, F., Issler, D., Forsberg, C.F., 2019. Landslide material control on tsunami genesis—The Storegga slide and tsunami (8100 years BP). J. Geophys. Res. Oceans 124 (6), 3607–3627. http://dx.doi.org/10.1029/2018JC014893.

Kim, J., Pedersen, G.K., Løvholt, F., LeVeque, R.J., 2017. A Boussinesq type extension of the GeoClaw model - a study of wave breaking phenomena applying dispersive long wave models. Coast. Eng. 122, 75–86.

Kirby, J.T., 2016. Boussinesq models and their application to coastal processes across a wide range of scales. J. Waterw. Port Coast. Ocean Eng. 142 (6), 03116005. http://dx.doi.org/10.1061/(ASCE)WW.1943-5460.0000350.

Kirby, J.T., Grilli, S.T., Zhang, C., Horrillo, J., Nicolsky, D., Liu, P.L.-F., 2018. The NTHMP Landslide Tsunami Benchmark Workshop, Galveston, January 9-11, 2017. Research Repor CACR-18-01, Center for Applied Coastal Research, Department of Civil and Environmental Engineering, University of Delaware, Newark, DE.

Kirby, J.T., Shi, F., Nicolsky, D., Misra, S., 2016. The 27 April 1975 Kitimat, British Columbia submarine landslide tsunami: A comparison of modeling approaches. Landslides 13, 1421–1434. http://dx.doi.org/10.1007/s10346-016-0682-x.

Kirby, J.T., Shi, F., Tehranirad, B., Harris, J.C., Grilli, S.T., 2013. Dispersive tsunami waves in the ocean: Model equations and sensitivity to dispersion and Coriolis effects. Ocean Model. 62, 39–55. http://dx.doi.org/10.1016/j.ocemod.2012.11.009.

Liu, P.L.-F., Higuera, P., Husrin, S., Prasetya, G., Prihantono, J., Diastomo, H., Pryambodo, D., Susmoro, H., 2020. Coastal landslides in Palu Bay during 2018 Sulawesi earthquake and tsunami. Landslides http://dx.doi.org/10.1007/s10346-020-01417-3.

Liu, P.L.-F., Wu, T.-R., Raichlen, F., Synolakis, C.E., Borrero, J.C., 2005. Runup and rundown generated by three-dimensional sliding masses. J. Fluid Mech. 536, 107–144. http://dx.doi.org/10.1017/S0022112005004799.

López-Venegas, A., ten Brink, U., Geist, E., 2008. Submarine landslide as the source for the October 11, 1918 Mona Passage tsunami: Observations and modeling. Mar. Geol. 254 (1), 35–46.

López-Venegas, A., Horrillo, J., Pampell-Manis, A., Huérfano, V., Mercado, A., 2015. Advanced tsunami numerical simulations and energy considerations by use of 3D–2D coupled models: the October 11, 1918, Mona Passage Tsunami. Pure Appl. Geophys. 172 (6), 1679–1698.

Løvholt, F., Bondevik, S., Laberg, J.S., Kim, J., Boylan, N., 2017. Some giant submarine landslides do not produce large tsunamis. Geophys. Res. Lett. 44 (16), 8463–8472. http://dx.doi.org/10.1002/2017GL074062.

Løvholt, F., Glimsdal, S., Harbitz, C.B., 2020. On the Landslide Tsunami Uncertainty and Hazard. Springer.

Løvholt, F., Pedersen, G., Gisler, G., 2008. Oceanic propagation of a potential tsunami from the La Palma Island. J. Geophys. Res. 113 (C09026), http://dx.doi.org/10.1029/2007JC004603.

Løvholt, F., Pedersen, G., Harbitz, C.B., Glimsdal, S., Kim, J., 2015. On the characteristics of landslide tsunamis. Phil. Trans. R. Soc. A 373, 20140376. http://dx.doi.org/10.1098/rsta.2014.0376.

Løvholt, F., Schulten, I., Mosher, D., Harbitz, C., Krastel, S., 2019. Modelling the 1929 grand banks slump and landslide tsunami. Geol. Soc. London Spec. Publ. 477 (1), 315–331.

Lynett, P.J., 2006. Nearshore wave modeling with high-order Boussinesq-type equations. J. Waterw. Port Coast. Ocean Eng. 132 (5), 348–357. http://dx.doi.org/10.1061/(ASCE)0733-950X(2006)132:5(348).

Lynett, P., Liu, P.F., 2002. A numerical study of submarine landslide-generated waves and runup. Proc. R. Soc. Lond. Ser. A Math. Phys. Eng. Sci. 458 (2028), 2885–2910. http://dx.doi.org/10.1098/rspa.2002.0973.

Lynett, P., et al., et 37 alia, 2017. Inter-model analysis of tsunami-induced coastal currents. Ocean Model. 114, 14–32. http://dx.doi.org/10.1016/j.ocemod.2017.04.003.

Ma, G., Kirby, J.T., Hsu, T.-J., Shi, F., 2015. A two-layer granular landslide model for tsunami wave generation: Theory and computation. Ocean Model. 93, 40–55. http://dx.doi.org/10.1016/j.ocemod.2015.07.012.

Ma, G., Kirby, J.T., Shi, F., 2013. Numerical simulation of tsunami waves generated by deformable submarine landslides. Ocean Model. 69, 146–165. http://dx.doi.org/10.1016/j.ocemod.2013.07.001.

Ma, G., Shi, F., Kirby, J.T., 2012. Shock-capturing non-hydrostatic model for fully dispersive surface wave processes. Ocean Model. 43–44, 22–35. http://dx.doi.org/10.1016/j.ocemod.2011.12.002.

Macías, J., Escalante, C., Castro, M.J., 2021a. Multilayer-HySEA model validation for landslide generated tsunamis. Part I Rigid slides. Nat. Hazards Earth Syst. Sci. 21, 775–789. http://dx.doi.org/10.5194/nhess-21-775-2021.

Macías, J., Escalante, C., Castro, M.J., 2021b. Multilayer-HySEA model validation for landslide generated tsunamis. Part II Granular slides. Nat. Hazards Earth Syst. Sci. 21, 791–805. http://dx.doi.org/10.5194/nhess-21-791-2021.

Macías, J., Vázquez, J., Fernández-Salas, L., González-Vida, P., Castro, M.J., Díaz-del Río, V., Alonso, B., 2015. The Al-Boraní submarine landslide and associated tsunami. A modelling approach. Mar. Geol. 361, 79–95. http://dx.doi.org/10.1016/j.margeo.2014.12.006.

McMurtry, G.M., Fryer, G.J., Tappin, D.R., Wilkinson, I.P., Williams, M., Fietzke, J., Garbe-Schoenberg, D., Watts, P., 2004. Megatsunami deposits on Kohala volcano, Hawaii, from flank collapse of Mauna Loa. Geology 32 (9), 741–744.

Mendoza, C.I., Santamaria-Holek, I., 2009. The rheology of hard sphere suspensions at arbitrary volume fractions: An improved differential viscosity model. J. Chem. Phys. 130 (4), 044904.

Mohammed, F., Fritz, H.M., 2012. Physical modeling of tsunamis generated by three-dimensional deformable granular landslides. J. Geophys. Res. 117 (C11015), http://dx.doi.org/10.1029/2011JC007850.

Nicolsky, D., Suleimani, E.N., Haeussler, P.J., Ryan, H.F., Koehler, R.D., Combellick, R.A., Hansen, R.A.,

Paris, A., Okal, E.A., Guérin, C., Heinrich, P., Schindelé, F., Hébert, H., 2019. Numerical modeling of the June 17, 2017 landslide and tsunami events in Karrat Fjord, West Greenland. Pure Appl. Geophys. 176 (7), 3035–3057.

Parsons, T., Geist, E.L., Ryan, H.F., Lee, H.J., Haeussler, P.J., Lynett, P., Hart, P.E., Sliter, R., Roland, E., 2014. Source and progression of a submarine landslide and tsunami: The 1964 Great Alaska earthquake at Valdez. J. Geophys. Res. Solid Earth 119, 8502–8516. http://dx.doi.org/10.1002/2014JB011514.

Plafker, G., Kachadoorian, R., Eckel, E.B., Mayo, L.R., 1969. Effects of the Earthquake of March 27, 1964 on Various Communities. Geological Survey Professional Paper 542-G, United States Dept. of Interior - Geological Survey.

Popinet, S., 2003. Gerris: a tree-based adaptive solver for the incompressible Euler equations in complex geometries. J. Comput. Phys. 190, 572–600. http://dx.doi.org/10.1016/S0021-9991(03)00298-5.

Ramalho, R., Winckler, G., Madeira, J., Helffrich, G., Hipólito, A., Quartau, R., Adena, K., Schaefer, J., 2015. Hazard potential of volcanic flank collapses raised by new megatsunami evidence. Sci. Adv. 1 (9), e1500456.

Rauter, M., 2021. The compressible granular collapse in a fluid as a continuum: validity of a Navier–Stokes model with $\mu(J), \phi(J)$ rheology. J. Fluid Mech. 915, A87. http://dx.doi.org/10.1017/jfm.2021.107.

Roeber, V., Cheung, K.F., Kobayashi, M.H., 2010. Shock-capturing Boussinesq-type model for nearshore wave processes. Coast. Eng. 57 (4), 407–423. http://dx.doi.org/10.1016/j.coastaleng.2009.11.007.

Salmanidou, D., Guillas, S., Georgiopoulou, A., Dias, F., 2017. Statistical emulation of landslide-induced tsunamis at the Rockall Bank, NE atlantic. Proc. R. Soc. Lond. Ser. A Math. Phys. Eng. Sci. 473 (2200), 20170026.

Sassa, K., Dang, K., Yanagisawa, H., He, B., 2016. A new landslide-induced tsunami simulation model and its application to the 1792 Unzen-Mayuyama landslide and tsunami disaster. Landslides 13 (6), 1405–1419.

Schambach, L., Grilli, S.T., Kirby, J.T., Shi, F., 2019. Landslide tsunami hazard along the upper US East Coast: effects of slide deformation, bottom friction, and frequency dispersion. Pure Appl. Geophys. 176 (7), 3059–3098. http://dx.doi.org/10.1007/s00024-018-1978-7.

Schambach, L., Grilli, S.T., Tappin, D.R., Gangemi, M.D., Barbaro, G., 2020. New simulations and understanding of the 1908 messina tsunami for a dual seismic and deep submarine mass failure source. Mar. Geol. 421, 106093. http://dx.doi.org/10.1016/j.margeo.2019.106093.

Schulten, I., Mosher, D.C., Piper, D.J.W., Krastel, S., 2019. A massive slump on the St. Pierre Slope, a new perspective on the 1929 Grand Banks submarine landslide. J. Geophys. Res. Solid Earth 124 (8), 7538–7561.

Sepúlveda, S., Serey, A., 2009. Tsunamigenic, earthquake-triggered rock slope failures during the April 21 2007 Aisén earthquake, southern Chile (45.5° S). Andean Geol. 26 (1), 131–136.

Shi, F., Kirby, J.T., Harris, J.C., Geiman, J.D., Grilli, S.T., 2012. A high-order adaptive time-stepping TVD solver for Boussinesq modeling of breaking waves and coastal inundation. Ocean Model. 43–44, 36–51. http://dx.doi.org/10.1016/j.ocemod.2011.12.004.

Si, P., Shi, H., Yu, X., 2018a. A general numerical model for surface waves generated by granular material intruding into a water body. Coast. Eng. 142, 42–51.

Si, P., Shi, H., Yu, X., 2018b. Development of a mathematical model for submarine granular flows. Phys. Fluids 30 (8), 083302.

Smith, R., Sprinks, T., 1975. Scattering of surface waves by a conical island. J. Fluid Mech. 72 (2), 373–384.

Snelling, B., Neethling, S., Horsburgh, K., Collins, G., Piggott, M., 2020. Uncertainty quantification of landslide generated waves using gaussian process emulation and variance-based sensitivity analysis. Water 12 (2), 416.

Stelling, G.S., Zijlema, M., 2003. An accurate and efficient finite-difference algorithm for non-hydrostatic free-surface flow with application to wave propagation. Internat. J. Numer. Methods Fluids 43, 1–23. http://dx.doi.org/10.1002/fld.595.

Svennevig, K., Dahl-Jensen, T., Keiding, M., Merryman Boncori, J., Larsen, T., Salehi, S., Munck Solgaard, A., Voss, P., 2020. Evolution of events before and after the 17 June 2017 rock avalanche at Karrat Fjord, West Greenland – a multidisciplinary approach to detecting and locating unstable rock slopes in a remote arctic area.. Earth Surf. Dyn. 8, 1021–1038.

Tappin, D.R., Grilli, S.T., Harris, J.C., Geller, R.J., Masterlark, T.L., Kirby, J.T., Shi, F., Ma, G., Thingbaijamg, K.K.S., Mai, P.M., 2014. Did a submarine landslide contribute to the 2011 Tohoku tsunami? Mar. Geol. 357, 344–361. http://dx.doi.org/10.1016/j.margeo.2014.09.043.

Tappin, D.R., Watts, P., Grilli, S.T., 2008. The Papua New Guinea tsunami of 17 July 1998: anatomy of a catastrophic event. Nat. Hazards Earth Syst. Sci. 8, 243–266.

Tehranirad, B., Harris, J.C., Grilli, A.R., Grilli, S.T., Abadie, S., Kirby, J.T., Shi, F., 2015. Far-field tsunami hazard in the north Atlantic basin from large scale flank collapses of the Cumbre Vieja volcano, La Palma. Pure Appl. Geophys. 172 (12), 3589–3616. http://dx.doi.org/10.1007/s11069-014-1522-8.

Torrence, C., Campo, G.P., 1998. A practical guide to wavelet analysis. Bull. Am. Meteorol. Soc. 79, 61–78.

Urgeles, R., Camerlenghi, A., 2013. Submarine landslides of the mediterranean sea: Trigger mechanisms, dynamics, and frequency-magnitude distribution. J. Geophys. Res. Earth Surf. 118 (4), 2600–2618.

Viroulet, S., Sauret, A., Kimmoun, O., 2014. Tsunami generated by granular collapse down a rough inclined plane. Eur. Phys. Lett. 105 (3), 34004. http://dx.doi.org/10.1209/0295-5075/105/34004.

Ward, S.N., Day, S., 2001. Cumbre Vieja volcano – potential collapse and tsunami at La Palma, Canary Islands. Geophys. Res. Lett. 28 (17), 3397–3400.

Watts, P., Grilli, S.T., Kirby, J.T., Fryer, G.J., Tappin, D.R., 2003. Landslide tsunami case studies using a Boussinesq model and a fully nonlinear tsunami generation model. Nat. Hazards Earth Syst. Sci. 3, 391–402.

Watts, P., Grilli, S.T., Tappin, D.R., Fryer, G.J., 2005. Tsunami generation by submarine mass failure Part II : Predictive equations and case studies. J. Waterw. Port Coast. Ocean Eng. 131 (6), 298–310. http://dx.doi.org/10.1061/(ASCE)0733-950X(2005)131:6(298).

Wei, G., Kirby, J.T., Grilli, S.T., Subramanya, R., 1995. A fully nonlinear bousinesq model for surface waves. Part 1. Highly nonlinear unsteady waves. J. Fluid Mech. 294, 71–92.

Weiss, R., Fritz, H.M., Wuennemann, K., 2009. Hybrid modeling of the mega-tsunami runup in Lituya Bay after half a century. Geophys. Res. Lett. 36, L09602. http://dx.doi.org/10.1029/2009GL037814.

Wilson, B., Torum, A., 1972. The Great Alaska Earthquake of 1964:. National Academy of Sciences - Engineering, Washington DC, pp. 361– 526..

Yamazaki, Y., Cheung, K.F., Kowalik, Z., 2011. Depth-integrated, non-hydrostatic model with grid-nesting for tsunami generation, propagation and run-up. Internat. J. Numer. Methods Fluids 67, 2081–2107. http://dx.doi.org/10.1002/fld.2485.

Yavari-Ramshe, S., Ataie-Ashtiani, B., 2016. Numerical modeling of subaerial and submarine landslide generated tsunami waves - recent advances and future challenges. Landslides 13 (6), 1325–1368. http://dx.doi.org/10.1007/s10346-016-0734-2.

Yavari-Ramshe, S., Ataie-Ashtiani, B., 2017. A rigorous finite volume model to simulate subaerial and submarine landslide generated waves. Landslides 14 (1), 203–221. http://dx.doi.org/10.1007/s10346-015-0662-6.

Zengaffinen, T., Løvholt, F., Pedersen, G.K., Muhari, A., 2020. Modelling 2018 anak krakatoa flank collapse and tsunami–effect of landslide failure mechanism and dynamics on tsunami generation. Pure Appl. Geophys. http://dx.doi.org/10.1007/s00024-020-02489-x.

Zhang, C., Kirby, J.T., Grilli, S.T., Ma, G., Shi, F., Shelby, M., 2017. NTHMP Landslide Benchmark Results for NHWAVE, Version 3.0. Research Report CACR-17-05, University of Delaware, Center for Applied Coastal Research, Department of Civil and Environmental Engineering.

Zhang, C., Kirby, J.T., Shi, F., Ma, G., Grilli, S.T., 2021a. A two-layer non-hydrostatic landslide model for tsunami generation on irregular bathymetry. 1. Theoretical basis.. Ocean Model. 159, 101749. http://dx.doi.org/10.1016/j.ocemod.2020.101749.

Zhang, C., Kirby, J.T., Shi, F., Ma, G., Grilli, S.T., 2021b. A two-layer non-hydrostatic landslide model for tsunami generation on irregular bathymetry. 2. Numerical discretization and model validation.. Ocean Model. 160, 101769. http://dx.doi.org/10.1016/j.ocemod.2021.101769.